Interpretation of the Top-Antitop-Photon Production Rate in Effective Field Theories

A Thesis

submitted to

Indian Institute of Science Education and Research Pune

in partial fulfillment of the requirements for the

BS-MS Dual Degree Programme

by

Sreelakshmi J S

Indian Institute of Science Education and Research, Pune

Dr. Homi Bhabha Road,

Pashan, Pune 411008, INDIA

April 2020

Supervisor: Prof. Dr. Arnulf Quadt,

Georg August Universität Göttingen, Germany

Certificate

This is to certify that this dissertation entitled Interpretation of the Top-Antitop-Photon Production Rate in Effective Field Theories towards the partial fulfilment of the BS-MS dual degree programme at the Indian Institute of Science Education and Research, Pune represents study/work carried out by Sreelakshmi J S under the supervision of Prof. Dr. Arnulf Quadt, Professor of Physics, II.Physikalisches Institut, Georg-August-Universität Göttingen, during the academic year 2019-2020.

Supervisor

Prof. Dr. Arnulf Quadt

Prof. Dr. Arnulf Quadt
Georg-August-Universität Göttingen
II. Physikalisches Institut
Friedrich-Hund-Platz 1
37077 Göttingen
aquadt@uni-goettingen.de

Sreelakshmi JS

Committee:

Prof. Dr. Arnulf Quadt

Dr. Sourabh Dube

Declaration

I hereby declare that the matter embodied in the report entitled *Interpretation of the Top-Antitop-Photon Production Rate in Effective Field Theories*, are the results of the work carried out by me at the II. Institute of Physics, Georg-August-Universität Göttingen, under the supervision of Prof. Dr. Arnulf Quadt, and the same has not been submitted elsewhere for any other degree.

Supervisor:

Prof. Dr. Arnulf Quadt

Prof. Dr. Arnulf Quadt
Georg-August-Universität Göttingen
II. Physikalisches Institut
Friedrich-Hund-Platz 1
37077 Göttingen
aquadt@uni-goettingen.de

Sreelakshmi J S

Acknowledgement

First of all, I would like to thank my supervisor, Prof. Dr. Arnulf Quadt, for giving me the opportunity to work with his group on this very exciting analysis. I am extremely grateful for the trust and confidence he placed on me and for his constant encouragement and motivation to understand the fundamentals of particle physics.

I also wish to express my heartfelt gratitude to Dr. Sourabh Dube for helping me channel my interest in particle physics and for being my mentor for the past three years. Thank you for being there to support and advice me whenever I was confused.

I am incredibly thankful to Dr. Thomas Peiffer for his constant guidance and handholding support throughout my project and for always being available for discussions. Special thanks to Steffen Korn for proofreading my thesis and for all the helpful comments.

My sincere thanks to the international office at the University of Goettingen for selecting me for the NAMASTE+ mobility program which funded my travel and stay at Goettingen.

Finally, thanks to my family and friends for their support and encouragement throughout, without which all of this would not have been possible.

Abstract

The top quark, the heaviest elementary particle, was discovered about 25 years ago. However, many of its fundamental properties, including the nature of its gauge couplings, are not yet accurately determined. The Standard Model (SM) predicts the top-photon vertex to be vectorially coupled. Given that the SM does not explain all observed phenomena, this analysis looks for additional axial-vector or tensor couplings using the Standard Model Effective Field Theory (SMEFT) approach. Three EFT operators that can affect the top-photon vertex are added to the SM Lagrangian with a coupling coefficient. By varying contributions from these three operators, 27 Monte Carlo samples are generated for the $t\bar{t}\gamma$ process. Changes were observed in the shape of the distribution of various kinematic variables like the p_{T}, η of the photon, $\Delta R_{min}(\gamma,\ell)$, $\Delta\phi(\ell,\ell)$ and $\Delta\eta(\ell,\ell)$. The differential cross-sections with respect to these observables are modelled as a second order polynomial function of the coupling coefficients to interpolate between the generated SMEFT $t\bar{t}\gamma$ samples. With these polynomial functions, limits are extracted on the coupling coefficients, namely C_{tW}, C_{tZ} and C_{tG}, from the differential cross-section measurements using the full run 2 data ($\mathscr{L} = 139$ fb^{-1}), from the ATLAS detector at the Large Hadron Collider.

Contents

List of Figures

List of Tables

1. Introduction

The curiosity to understand the way of nature has been intriguing humankind from the ancient times. Many speculations about what everything is composed of have been made by philosophers and thinkers like Democritus dating back to a few 100 BC. However, the first experimental evidence of a fundamental particle was made in 1897 when J. J. Thomson discovered the electron [1] and made the first proposal for a model of an atom. Around 1910, H. Geiger and E. Rutherford, hypothesised the existence of a nucleus in an atom, based on their alpha particle scattering experiment [2], and in 1914 Niels Bohr named the proton and proposed the orbital model of the hydrogen atom [3]. The discovery of the neutron by Chadwick in 1932 [4] gave a sort of complete idea that matter is composed of protons, electrons and neutrons. Around the 1940s, observation of cosmic rays revealed the existence of muons [5] which demanded the need for an improvement on the existing theory. Further, during the 1950s a large number of new particles was observed, and the process of incorporating all of them into a fundamental theory led to the birth of the Standard Model (SM) of particle physics.

The SM [6–16] (Section 2.1) is the most successful attempt till date at making one full theory to explain the fundamental nature of the universe. A large number of predictions made by the SM have been proven experimentally. This includes the discovery of the top quark [17, 18] and the Higgs boson [19, 20]. Due to the massive nature of these particles, they can only be observed in high energy collider experiments like the TEVATRON and the LHC. Despite being very accurate in its predictions, some observations cannot be explained by the SM (Section 2.2). Hence, the quest to find the fundamental theory of everything is still ongoing.

In the SM, the top quark decays before hadronisation (Section 2.1.1). Hence, the fundamental properties of a bare quark can be understood by studying the top quark. Precise measurements of its properties are the key to understanding the basic principles of nature, and this makes the top quark a good candidate for Beyond the Standard Model (BSM) studies. The process of top-antitop-quark production in association with a photon ($t\bar{t}\gamma$) allows for a measurement of the electromagnetic coupling of the top quark with a photon. A precise measurement of this coupling can help us to look for deviations from the SM.

The Standard Model Effective Field Theory (SMEFT) tries to explain these deviations by adding higher-dimensional operators to the SM Lagrangian. Limits can be obtained on the coupling strength of these operators using the measured inclusive and differential cross-section of the $t\bar{t}\gamma$ process. Due to the high top quark production cross-section at the Large Hadron Collider (LHC), the data collected over the years 2015-2018 at the ATLAS detector provides

the opportunity to study this rare process and extract these limits.

In this thesis, first, an introduction is given to the Standard Model in Section 2.1, here the fundamental particles and their interactions are explained. Then, the $t\bar{t}\gamma$ process is introduced in Section 2.1.1, with details on the special properties of the top quark. An introduction into Beyond the Standard Model physics is given in Section 2.2, with an emphasis on EFT and SMEFT. In Chapter 3, An overview of the LHC is given, and the working of the ATLAS detector is explained. The strategies used for generating events are explained in Chapter 4. In Chapter 5, steps taken to extract the limits are explained, and Chapter 6 summarises the results. Finally, Chapter 7 lists possible studies that can be undertaken to improve the results of this analysis.

2. Theoretical Background

This chapter gives a brief overview of some of the theoretical concepts that are necessary to understand this analysis.

2.1. Standard Model

Quantum Field Theory (QFT) is a mathematical framework that combines quantum mechanics, special relativity and classical field theory. The Standard Model of Particle Physics (SM) is a combination of three local gauge-invariant QFTs. It has an underlying symmetry group $SU(3)_C \times SU(2)_L \times U(1)_Y$, where, $SU(3)$ describes the strong interaction in the framework of Quantum Chromodynamics (QCD) and $SU(2)_L \times U(1)_Y$ describes the electro-weak interaction.

In the SM, particles are classified on the basis of their spin into fermions (particles with half-integer spins) and bosons (particles with integer spins). All matter is composed of fermions, and they interact through the exchange of elementary gauge bosons. These fermions are further divided into quarks and leptons. All the particles in the SM are displayed in Fig. 2.1. Corresponding to each of these particles there exists an anti-particle in the SM.

There are three generations of leptons, each consisting of a charged ($Q = -1e$) lepton (ℓ) and its uncharged weak isospin partner, a neutrino (ν_ℓ). The leptons in the three generations vary only in terms of their mass. The three generations are; electron (e) and electron neutrino (ν_e), muon (μ) and muon neutrino (ν_μ), and tauon (τ) and tauon neutrino (ν_τ). The charged leptons interact electro-weakly, while the neutrinos show only weak interactions.

There are six flavours of quarks. These are grouped into three generations. Each generation has two quarks, one up-type quark with weak isospin (I_3) of 1/2 and a down-type quark with $I_3 = -1/2$. Quarks in different generations show drastic variation in their mass as seen from Fig. 2.1. The first generation consists of the up (u) and the down (d) quarks, the second has the charm (c) and the strange (s) quarks, and the third includes the top (t) and the bottom (b) quarks. In addition to electric charge, quarks also have a colour charge which makes them interact through the electro-weak and the strong force. The colour charge is of three types, and all stable particles are composed of combinations of quarks such that the net colour is neutral.

The Standard Model describes three out of the four fundamental forces. The electromagnetic force is mediated by photons (γ) and is experienced by all electromagnetically charged particles. The gluon (g) is the force carrier particle for the strong force, and all coloured particles

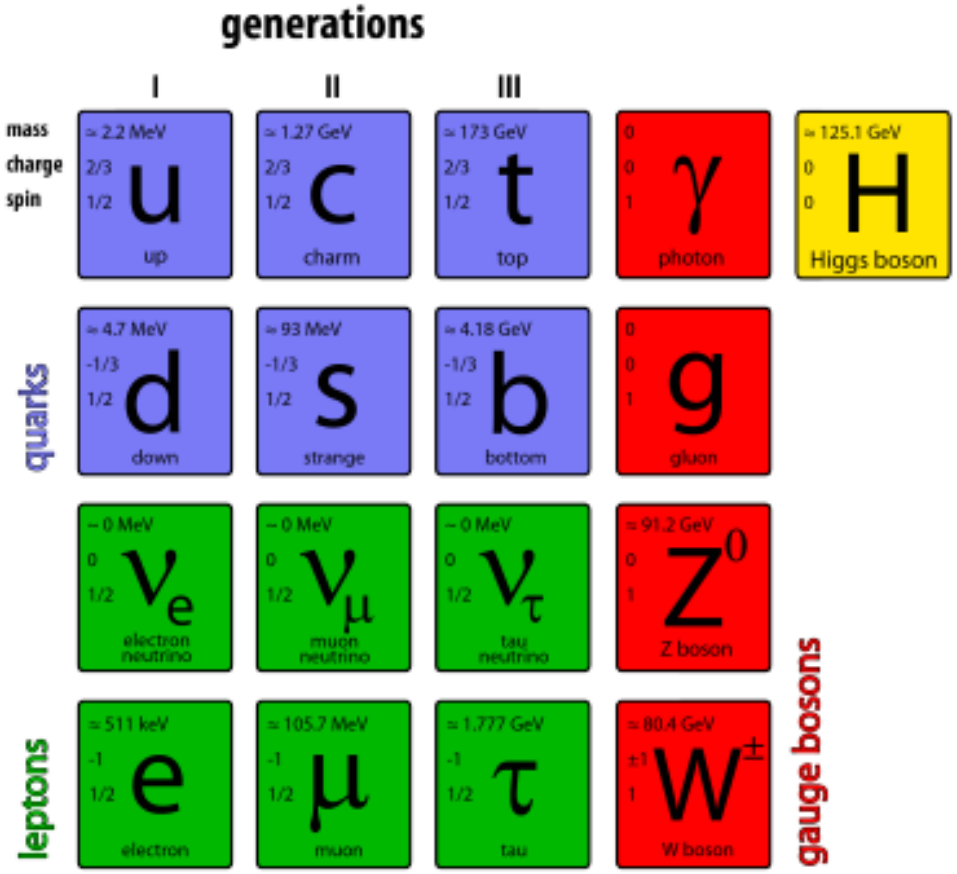

Figure 2.1.: The Standard Model of particle physics: an overview.

interact via the strong force. The weak force is mediated by $W^{\pm}$ and Z bosons. The electromagnetic force and the weak force are unified in the electro-weak theory. The gravitational force is not explained by the SM.

The Higgs boson is a massive ($m_H = 124.97 \pm 0.24\ GeV$ [21]) spin-zero [22] particle with no charge. It was introduced to the SM to explain the massive nature of other gauge bosons using the Brout-Englert-Higgs [23, 24] mechanism.

2.1.1. The top quark

The third generation of quarks was proposed by Kobayashi and Maskawa [25] in 1973 as an explanation to the CP violation observed by Cronin *et al.* [26] in the 1960s. The discovery of the τ lepton at SLAC [27] and the bottom-quark at FERMILAB [28] in 1977 strengthened the feasibility of the existence of a third generation, and hence the top quark. The top quark was first discovered by CDF and DØ in 1995 during the Run I at the TEVATRON [17, 29].

In the SM, the top quark is an up-type quark with spin $s = 1/2$ and charge $Q = +2/3e$. It is the heaviest quark observed, with a mass equal to 172.69 ± 0.48 GeV [30], which is 30 times more that the mass of the second heaviest quark. The mass distribution follows a Breit-Wigner

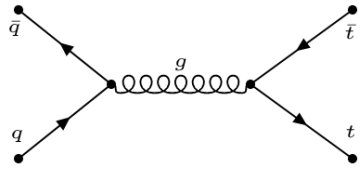

(a) From quark-anti-quark pairs

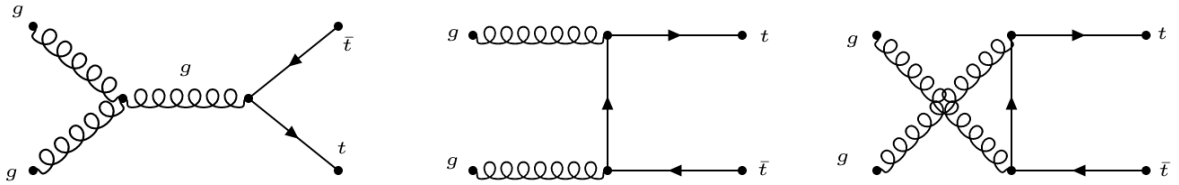

(b) From gluon-gluon fusion

Figure 2.2.: Leading-order diagrams for $t\bar{t}$ production at hadron colliders.

function, a statistical probability function which describes resonances in high energy physics. The lifetime is the inverse of the decay width (the full width at half maximum (FWHM)) of the mass distribution. Hence, it has a very short lifetime of about 10^{-25}s [31], which is shorter than the QCD hadronisation time. Because of this short lifetime, it decays before hadronisation can occur [31], and thus transfers its properties to its decay products. The properties of the top quark can be measured from its decay products, making it easier to study the top quark.

Top quark production

Top quarks can be produced as a single quark or a top anti-top pair ($t\bar{t}$). At the LHC, the top quark is mainly produced in pairs. A top anti-top pair can be produced either from gluon-gluon fusion or quark anti-quark annihilation, as shown in Fig. 2.2. The LHC is a proton-proton collider, and since protons are compound particles, during a collision, the partons that constitute the proton interact with each other and not the entire proton. Each parton has only a fraction (x) of the total energy of the proton, and this fraction is given by the parton distribution function [32], an example is shown in Fig. 2.3. To produce a real top-quark pair, it is required that the interacting partons have $\sqrt{\hat{s}} > 2m_t$. Given the centre of mass energy of the total collision is $\sqrt{s}$, $\sqrt{\hat{s}} = x\sqrt{s}$. At the LHC, the probability of obtaining a gluon is much higher than the probability of obtaining an anti-quark with a high enough x. Hence, about 90% of the $t\bar{t}$ events are produced through the $gg \rightarrow t\bar{t}$ process.

The production cross-section of a process can be calculated using the QCD factorisation theorem [33]. Consider the two interacting partons to be i and j, with a PDF f_i and f_j, respectively. The total cross-section can be computed from the partonic cross-section ($\sigma_{ij} \rightarrow t\bar{t}$) by convoluting it with the PDFs and summing over all combinations of partons feasible as shown in the equation below. The PDF is written as a function of x_i and Q^2, where, x_i is the fraction of the centre of mass energy carried by the parton and Q gives the factorisation scale.

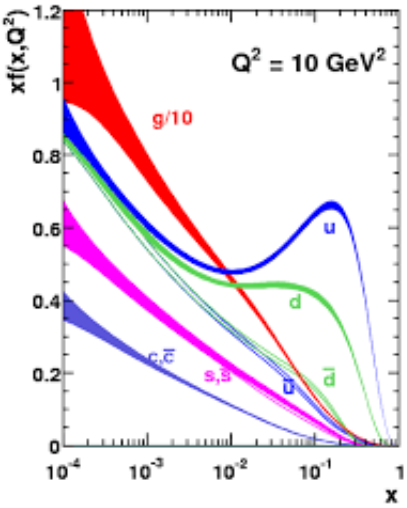

Figure 2.3.: Parton Distribution Function for $Q^2 = 10^4$ GeV.

$$\sigma_{t\bar{t}}(\sqrt{s}, m_t) = \sum \lim_{i,j=q,\bar{q},g} \int dx_i dx_j f_i(x_i, Q^2) f_j(x_j, Q^2) \times \hat{\sigma}_{ij\to t\bar{t}}(\hat{s}, x_i, x_j, m_t, Q, \alpha(Q^2)) \quad (2.1)$$

Top quark decay

The top quark decays almost exclusively to a W boson and a b quark. The rate of this decay can be calculated from the corresponding Cabibbo Kobayashi Maskawa (CKM) matrix elements. The CKM matrix elements contain information about the strength of flavour changing weak decays. The rate of the $t \to Wb$ decay is given by the following equation:

$$\mathscr{R} = \frac{\mathscr{B}(t\to Wb)}{\mathscr{B}(t\to Wq)} = \frac{|V_{tb}|^2}{\Sigma_q |V_{tq}|^2} \approx 1$$

Hence, the decay of the top quark is classified on the basis of the decay of the W boson. The W boson can decay into a quark anti-quark pair, or a charged lepton and its neutrino. In a $t\bar{t}$ event, based on the decay of the W boson, there are three decay channels. (i) All hadronic: both the W bosons decay into a quark and anti-quark. (ii) Dileptonic: both the quarks decay into a lepton pair. (iii) Semileptonic: one of the quarks decays leptonically and the other hadronically. The branching ratios for each of these channels are given in Fig. 2.4(b).

2.1.2. $t\bar{t}\gamma$ process

In Section 2.1.1, the production and decay modes of the $t\bar{t}$ pair are explained. For the $t\bar{t}\gamma$ process, the final states are similar to that of the $t\bar{t}$ process, with an additional prompt photon. This additional photon can have three different sources of origin. Some examples are shown in Fig 2.5.

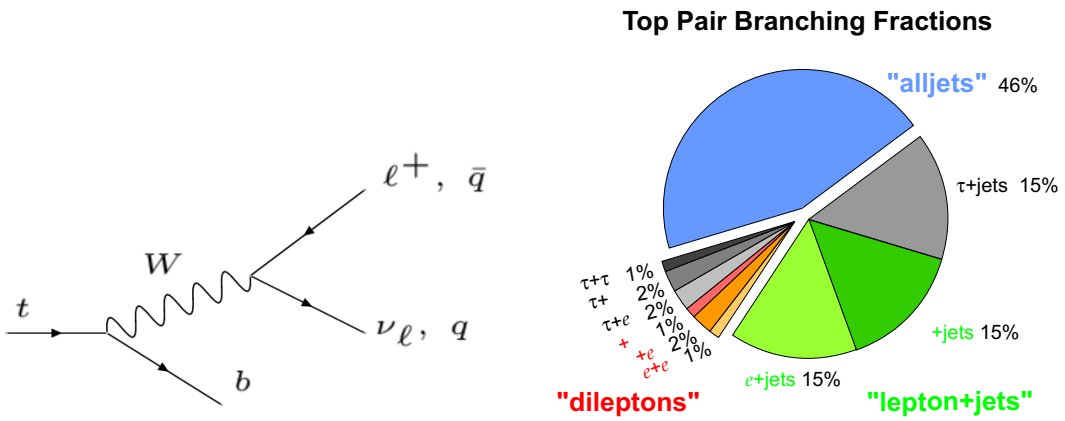

(a) Top quark decay (b) Branching ratio of $t\bar{t}$process

Figure 2.4.: Top quark decay and branching ratio.

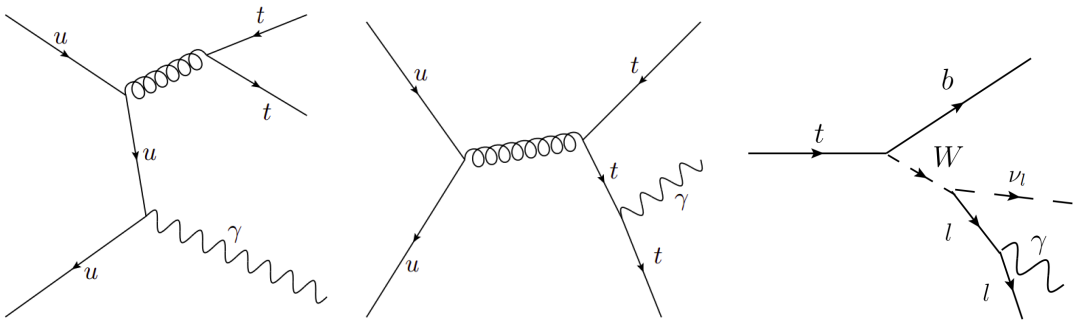

(a) ISR (b) from top quark (c) FSR

Figure 2.5.: Feynman diagrams of $t\bar{t}\gamma$ production.

The photon can be radiated from one of the initial state partons; this is called Initial State Radiation (ISR). As gluons cannot radiate a photon, the only contributors to this are processes where $t\bar{t}$ is produced from qq annihilation. At the LHC the fraction of $t\bar{t}$ events that are produced from qq annihilation is very low, and hence this channel has a very small contribution to the total number of events. The photon can also be radiated directly from the top quark. These events are important for studying the top-photon coupling. Another possibility is that the photon is radiated from one of the charged decay products of the top quark. These are called final-state radiation (FSR). The events that are most relevant for the study of the top-photon coupling are those where the photon is radiated directly from the top quark. These processes are hard to distinguish and have to be treated simultaneously with ISR and FSR processes. The FSR photons have lower isolation compared to the photons radiated by the top quark. This can be used to distinguish these events from the other $t\bar{t}\gamma$ events.

2.2. Beyond the Standard Model physics

In the current level of understanding that humankind has of the universe, all the observations at an energy scale of less than a few 100 GeV can be explained by the SM. But few observations are not understood within the SM. One such example is neutrino oscillations [34], which can be explained only if the neutrinos are considered to be massive. But according to the SM, neutrinos are massless. Some other examples of observations which are not explained by the SM are the matter anti-matter asymmetry [35], the existence of dark matter [36, 37] and dark energy [38]. Also, gravity is not explained by the SM.

Clearly, an improved theory or an extension of the SM is necessary to fulfil our quest of finding a theory of everything. Several attempts have been made in this direction, which includes alternative approaches to the SM, like string theory and extra dimensions. String theory uses one dimensional objects called strings to explain all fundamental particles and their interactions. At a scale larger that than of the string, these strings can be approximated to a particle, and the vibrational state of the string determines the charge, mass and other properties of this particle. In this approach, one of the vibrational states of the string corresponds to a particle like graviton, and this provides a unified theory that can explain gravity as well, unlike the SM. Another alternative approach aims to explain gravity and the hierarchy problem using extra dimensions beyond the observed space-time [39].

There are also theories which are extensions of the SM, for example, Supersymmetry (SUSY). SUSY attempts to solve the hierarchy problem by proposing a superpartner particle for each SM particle which differs from its partner only in terms of its spin. Since these additional light particles have not been observed, SUSY has to be broken in order to allow these superpartners to have a higher mass. Extensions of SM can also be done using Effective Field Theoretic approaches. This is explained in the next section.

2.2.1. Effective Field Theory (EFT)

An EFT [40] is a low energy/length scale approximation of an over-arching theory. Such an approximation does not include a detailed description of the theory at the higher energy sector. Hence, the EFT approach is a good tool to constrain an unknown over-arching theory that describes processes at both high and low energy scales using a known theory at the low energy scale. This approach works because the observables at one energy scale are not directly sensitive to the physics at a different scale.

An example: Fermi weak theory

An easy way to understand the power of EFT is through an example. In this example, the over-arching theory is the SM in which the exchange of W bosons (mass m_W) mediates the weak interaction. Consider the case of a muon decay, with a coupling constant g and a 4-momentum

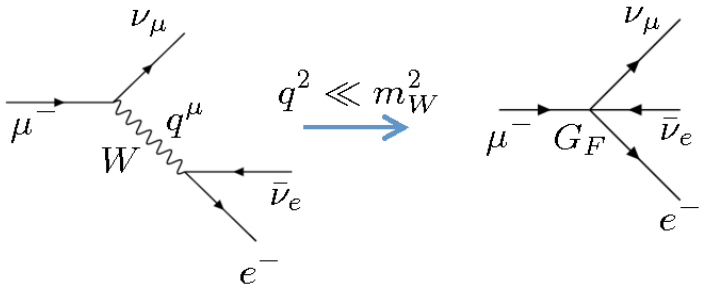

Figure 2.6.: A low energy approximation of a muon decay [41].

exchange q_μ through a W boson propagator, as shown in the left part of Fig. 2.6. The amplitude for this full process is:

$$\mathscr{M}_{full} \propto \frac{g^2}{q_2 - m_W^2} \tag{2.2}$$

If q_μ is small, the W boson can be replaced by a 4-fermion interaction as shown in Fig. 2.6 to obtain an effective theory. The amplitude for this process is given by:

$$\mathscr{M}_{full} \propto -\frac{g^2}{m_W^2} \tag{2.3}$$

These two amplitudes are equal when the momentum transfer is small. Hence, before the discovery of the W boson, Enrico Fermi in 1933 proposed this four fermion interaction model with the coupling constant G_f to explain the muon decay. Later on, with the discovery of the W boson, it was identified that G_f is equivalent to $\frac{g^2}{8m_W^2}$. Similarly, there could be other such interactions at very high energy scales, that can be approximated to a low energy EFT at the energy scales that are currently experimentally accessible. This gives the option to study BSM physics in a model independent manner.

2.2.2. Building an EFT

An EFT can be described as a sum of operators O_i with a specific mass dimension and a coupling constant in front of it. The coupling constant can be split into a dimensionless constant (Wilson coefficient, c_i), and a power of mass scale (Λ) at which the theory is written, as shown below:

$$\mathscr{L} = (\text{kinetic and mass terms}) + \sum_i \frac{c_i}{\Lambda^{D_i-4}} O_i \tag{2.4}$$

According to QFT, the action has to be dimensionless and hence each term in the Lagrangian has a mass dimension d = 4 in natural units ($\hbar$ = c = 1). Hence, given the dimension of the operator, the dimension of the coefficient can be calculated.

An EFT can be obtained using "top-down" or "bottom-up" approaches. A "top-down" approach is taken when a high-energy theory is known. In this case, a low-energy theory can be made by eliminating high energy effects. For example, the particles which are more massive than the energy scale of the effective theory can be omitted in this theory. This approach is used to simplify a theory when applied at low-energy scales.

In the case that a re-normalisable theory at high energy is not known, an attempt to identify this theory can be made using the "bottom-up" approach, by adding additional higher dimensional interactions. Using this method, an effective theory can be described at an energy scale E with an accuracy ε using a finite set of parameters to describe the interactions at each dimension $(k-4)$. The coefficients of each of these interaction terms is less than or of the order of:

$$\frac{1}{M^k} \text{ where } E < M \tag{2.5}$$

This is because the interactions of dimension k is proportional to

$$\left(\frac{E}{M}\right)^k \tag{2.6}$$

and hence for an accuracy of ε only terms up to dimension k_e are significant

$$\left(\frac{E}{M}\right)^{k_\varepsilon} \approx \varepsilon \implies k_\varepsilon \approx \frac{ln(1/\varepsilon)}{ln(M/E)} \tag{2.7}$$

k_ε is finite and increases with energy.

2.2.3. Standard Model Effective Field Theory (SMEFT)

In SMEFT, the SM is considered as a low energy approximation of a complete theory. This complete theory can be speculated using the bottom-up approach. Predictions are made on the additional terms that should be added to the SM Lagrangian to obtain the full theory by considering symmetries such as Lorentz and gauge symmetries. The SMEFT provides a model-independent approach to study deviations from the Standard Model. These deviations are explained using higher-dimensional operators (O_i), which are built from SM fields. These

operators modify the SM Lagrangian as per the following equation:

$$\mathscr{L} = \mathscr{L}_{SM} + \Delta\mathscr{L} = \mathscr{L}_{SM} + \Sigma_i \frac{C_i}{\Lambda^2} O_i + h.c. \tag{2.8}$$

In this equation, O_i is the operator, C_i is the corresponding Wilson coefficient, which determines the coupling strength of the operator and Λ corresponds to the energy scale under consideration.

The SMEFT model for top-quark physics

This analysis uses the SMEFT model called *dim6top* [42]. It is a leading order (LO) implementation of SMEFT operators that are relevant for top quark physics. It uses the Warsaw basis [43] of gauge-invariant dimension-six operators. A $U(2)_q \times U(2)_u \times U(2)_d$ symmetry is assumed between the first two generations of quarks. For simplicity, the CKM matrix is approximated to a unit matrix, and masses of all the particles other than the top and the bottom quarks are approximated to zero. For leptons, flavour diagonality is assumed, with a $U(1)_l \times U(1)_e$ diagonal subgroup for each of the three generations. From this model, for the study of the top-photon vertex, the relevant operators are chosen [44]. These are listed below:

$$\begin{aligned} O_{tG} &= y_t g_s (\bar{Q}\sigma^{\mu\nu} T^A t)\bar{\psi} G^A_{\mu\nu} \\ O_{tW} &= y_t g_w (\bar{Q}\sigma^{\mu\nu} \tau^I t)\bar{\psi} W^I_{\mu\nu} \\ O_{tB} &= y_t g_y (\bar{Q}\sigma^{\mu\nu} t)\bar{\psi} B_{\mu\nu} \\ O_{tZ} &= -sin(\theta_w) O_{tB} + cos(\theta_w) O_{tW} \end{aligned} \tag{2.9}$$

Here, y_t is the Top-Yukawa coupling, g_w, g_y, g_s are the SM gauge coupling constant, ψ is the Higgs field and Q denotes the Quark doublet. $W^I_{\mu\nu}$, $B_{\mu\nu}$ and $G^A_{\mu\nu}$ are the field tensors.

The operator O_{tZ} is a linear combination of the operators O_{tW} and O_{tB}, and θ_w is the weak mixing angle. Hence, for this study, O_{tG}, O_{tW} and O_{tZ} operators will be considered. As the operator has a dimension six, the energy scale has to be of the order two so that the new term added to the Lagrangian has a dimension four. In the *dim6top* model, the energy scale Λ has been set to 1 TeV.

3. Experimental Setup

Most of the fundamental particles in the Standard Model cannot be observed freely in nature. Hence, from early times, attempts have been made to design accelerators and detectors to create them in controlled environments to study their unique properties. Currently, the Large Hadron Collider (LHC) [45] at CERN (European Organization for Nuclear Research) is the most powerful particle accelerator in the world. At the LHC there are two general-purpose detectors, namely, the ATLAS (A Toroidal LHC ApparatuS [46]) and the CMS (Compact Muon Solenoid [47]) experiments as well as the two specialised experiments, the ALICE (A Large Ion Collider Experiment [48]) and the LHCb (Large Hadron Collider beauty experiment [49]). In this chapter an overview of the functioning of the LHC and the ATLAS detector is presented.

3.1. The Large Hadron Collider

The LHC is the largest particle accelerator ever built. It is a double ring synchrotron with an approximate circumference of 27 km. It is constructed within the Large Electron-Positron (LEP) tunnel and is located 100 m under the surface. The LHC is mainly designed as a proton-proton collider, with a maximum design centre of mass energy $\sqrt{s}$ of 14 TeV. Its construction was approved in 1994, and the first successful proton beam test run was done on 10th September 2008. To keep the beam within the beam pipe, superconducting magnets are used, which produces a magnetic field of 8.33T. To attain such high magnetic fields, the magnets are cooled to 1.9 K using liquid helium. 1232 superconducting dipole magnets are located along the LHC to keep the beam on track and 392 quadrupole magnets are used for focusing.

The two rings in the LHC consists of eight circular arcs and straight regions. The protons are accelerated in opposite directions in the two beams. These are collided at four interaction points, which hosts the detectors.

A chain of accelerators is used to increase the energy of the beam before it is injected into the main LHC tunnel. These are shown in Fig. 3.1. As a first step, electrons are removed from hydrogen atoms using an electric field. These protons are then accelerated to an energy of 50 MeV using a linear accelerator, LINAC2. During this, the beam is also split into bunches. These bunches are injected into the Proton Synchrotron Booster (PSB) which increases the energy to 1.4 GeV. The energy of the beam is further increased to 25 GeV by the Proton Synchrotron (PS) and finally, the Super Proton Synchrotron (SPS) accelerates the beam to an energy of 450 GeV, before it is injected into the main LHC tunnel.

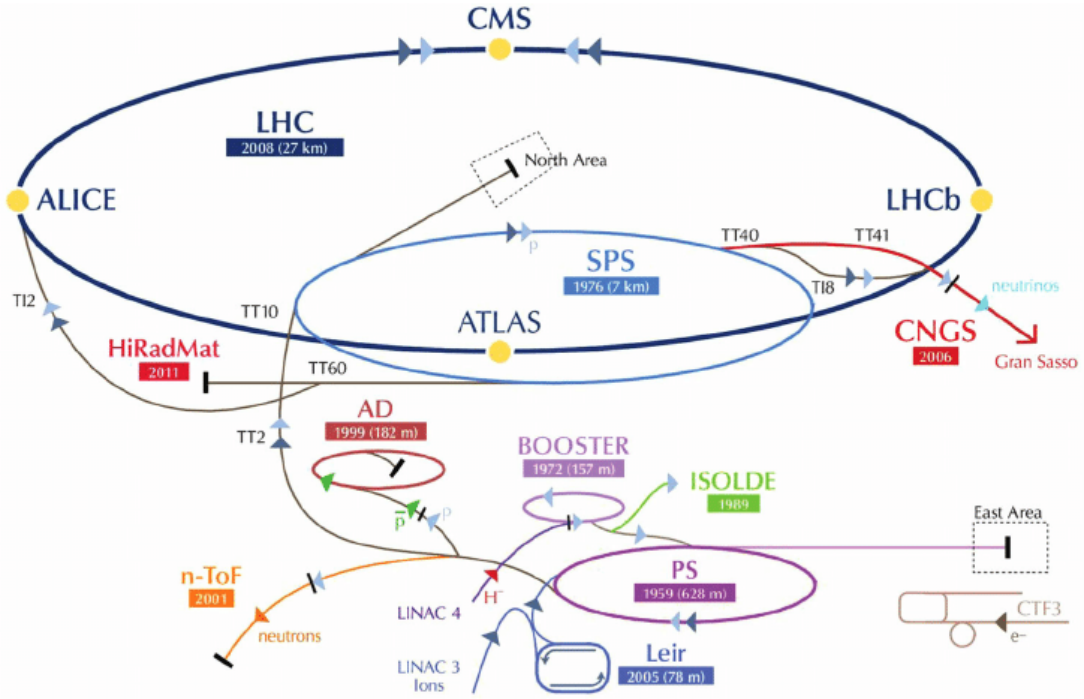

Figure 3.1.: The LHC accelerator complex © CERN.

The beam from the SPS is split into two parts, and each of these are injected into the two beam pipes of the LHC. Each of these beams contains 2808 bunches, with about 1.5×10^{11} protons per bunch. 16 radio-frequency cavities are used to further accelerate the protons to the desired final energy. The first high energy run started in March 2010 with $\sqrt{s} = 13$ TeV, which was then enhanced to $\sqrt{s}$ of 8 TeV in April 2012. This was further increased to $\sqrt{s} = 7$ TeV during the Run II of the LHC which started in June 2015. Currently, the LHC is in the long shutdown 2 and is expected to start running at its design energy of 14 TeV from spring 2021.

The LHC is designed to reach an instantaneous luminosity of $\mathscr{L} = 10^{34}$ cm^{-2} s^{-1}. The instantaneous luminosity can be calculated from the number of bunches (n_B), number of bunches per beam (N_1, N_2), frequency of revolution (f), and the beam size in x and y direction (σ_x and σ_y) using the following equation,

$$\mathscr{L} = \frac{n_b N_1 N_2 f}{4\pi\sigma_x\sigma_y} \tag{3.1}$$

Further, the number of events for a particular process with a cross-section, σ can be calculated as:

$$N = \sigma \int_t \mathscr{L} dt. \tag{3.2}$$

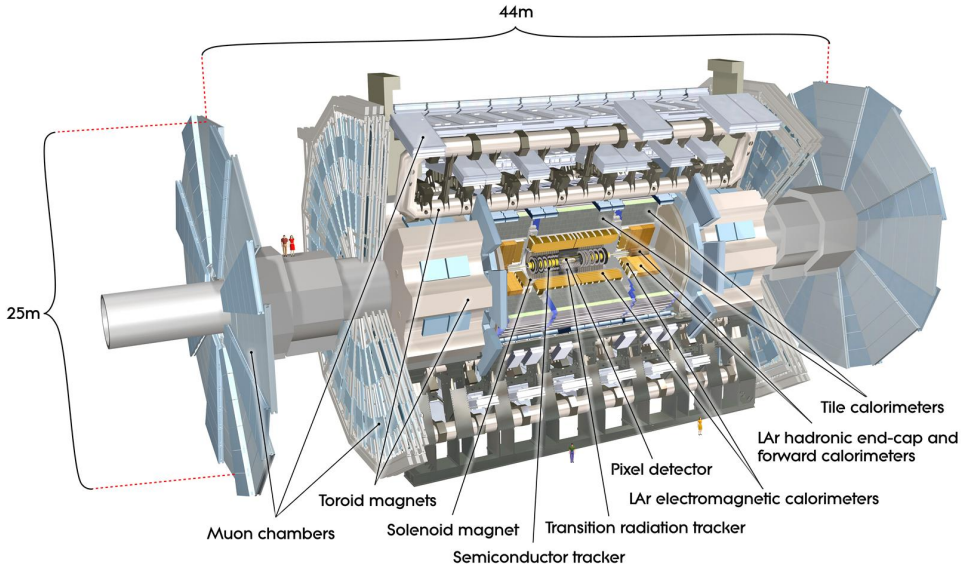

Figure 3.2.: The ATLAS detector © CERN.

3.2. The ATLAS detector

The ATLAS detector is 44 m in length, 25 m in diameter and has an overall weight of 7000 t. It is the largest detector in volume ever constructed for accelerator-based particle physics. A schematic of the ATLAS detector is shown in Fig. 3.2. The ATLAS detector consists of three main detector components: the Inner Detector (ID), the calorimeter system, and the muon spectrometer. It also has several toroidal and solenoid shaped magnets to bend the tracks of the charged particles produced in a collision. Fig. 3.3 shows details on how different particles can be identified based on the signatures they leave in the ATLAS detector.

3.2.1. Inner Detector

The primary purpose of the ID is to reconstruct the tracks of the charged particles. With this information, the charge and the momentum of the charged particles can be computed. For this, the ID is composed of three sub-systems. The innermost layer close to the beam pipe is the pixel detector, which is composed of three barrel-shaped layers, three additional disks on each end and an Insertable B Layer (IBL). It consists of about 80 million silicon semiconductor pixels with a minimum size of $50 \times 400\,\mu m^2$. Electron-hole pairs are produced when a charged particle travels through the pixel. The electrical signals produced can be measured to identify the location of the charged particle with a resolution of $14 \times 115\,\mu m^2$ around the interaction point.

The Semiconductor Tracker (SCT) surrounds the inner detector. It consists of four barrel layers and a total of eighteen endcaps, which are made of single-sided p-in-n microstrips instead of pixels and can achieve a resolution of 17 µm.

The SCT is surrounded by the Transition Radiation Tracker (TRT). The TRT is made of narrow tubes (diameter = 4 mm), filled with a gas mixture of Xe, CO_2, and O_2. A 0.03 mm thin gold-plated tungsten wire is placed in the centre. Charged particles ionise the gas while passing through it and the electrons produced undergo avalanche multiplication close to the wire. The position of the particle is determined by measuring the current.

3.2.2. Calorimeters

The second major component of the detector is the calorimeter system. It consists of the electromagnetic and the Hadronic Calorimeter. Each of these have an absorber and an active medium. It measures the energy of electrons, photons and jets by creating a particle shower in the absorber, till the total energy of the particle is deposited. The active medium converts these deposits into a detectable signal.

There are two main types of calorimeters. The Electromagnetic Calorimeter (ECAL) measures the energy deposited by photons and electrons. It uses lead as the absorber and liquid argon (LAr) as the active medium and has a barrel part and two end-caps. A particle shower in ECAL mainly happens due to bremsstrahlung and pair production, hence other particles pass through with very less energy losses. The coverage of the ECAL is up to $|\eta| < 3.2$. The ATLAS Hadronic Tile Calorimeter surrounds the ECAL and measures the energy of the jets (coming from hadrons). Steel is used as the absorber and the scintillating tiles act as the active medium in the barrels, while copper and LAr are used as the absorber and active medium respectively in the Hadronic End-Cap Calorimeter. The tile calorimeter covers a range of $0 < |\eta| < 1.7$ and the End-Cap calorimeter spans the region between $1.5 < |\eta| < 3.2$.

3.2.3. Muon chamber

Muons pass through the tracker and the calorimeters without much energy loss. This is because the probability to radiate bremsstrahlung is inversely proportional to the square of the mass of the particle and muons are about 200 times more massive than electrons. Muons are bent by the magnetic field produced by a toroidal magnet system and by measuring their trajectories, their charge and momentum are determined. The muon detector consists of Thin Gap Chambers (TGC), Resistive Plate Chambers (RPC), Monitored Drift Tubes (MDT), and Cathode Strip Chambers (CSC).

3.2.4. Trigger system

At the LHC, a bunch crossing happens once every 25 ns. A large number of the proton-proton collisions are not interesting for most physics analysis. It is not possible to record all the collision information and is not necessary. Hence, a trigger system [50] is installed to select only

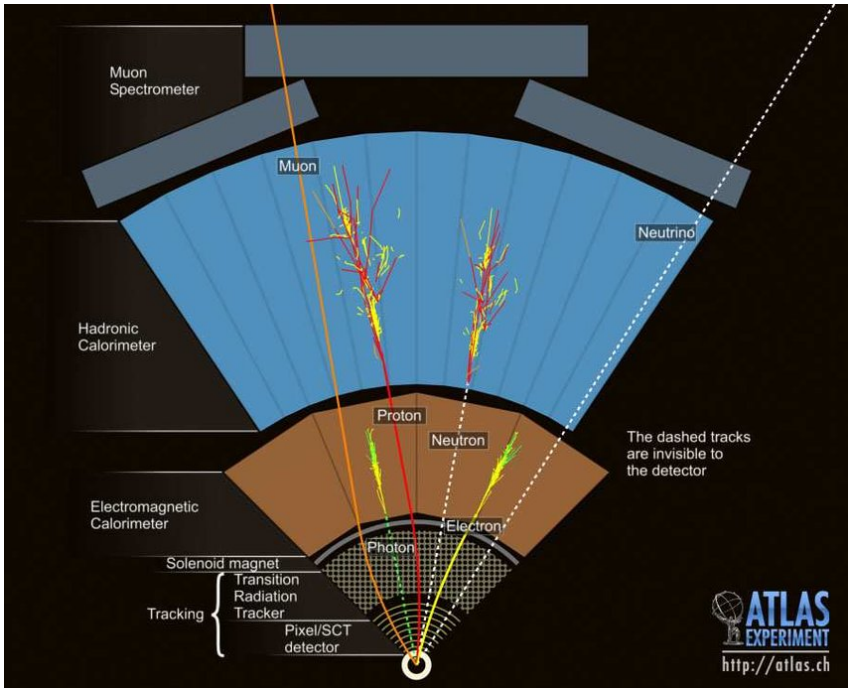

Figure 3.3.: A schematic of energy deposits and tracks as observed at the ATLAS detector © CERN.

the events that could include some 'interesting' physics observations. Two levels of trigger reduce the data collection rate from 40 MHz to 1 MHz. The first Level 1 trigger uses information from calorimeters and muon chambers to attain this. This is further reduced to about 1 KHz by the High-Level Trigger. In the ATLAS detector, Level 1 trigger is hardware based, and the High-Level Trigger is run on a computing cluster.

3.2.5. Coordinate System

A cylindrical coordinate system is used to label particles within the detector. In this system, the origin is at the interaction point of the two beams, which happens at the centre of the detector. The z-axis is along the beam pipe. The azimuthal angle ϕ determines the position in the transverse plane, with the zero set to the direction pointing to the centre of the ring. The other polar angle θ is measured in the plane perpendicular to the ring, with the baseline along the direction of the beam pipe. Commonly, the pseudorapidity (η) is used instead of the polar angle θ and it is defined as:

$$\eta = -\ln\left[\tan\left(\frac{\theta}{2}\right)\right]. \tag{3.3}$$

4. Sample preparation

MADGRAPH [51] is a Next-to-Leading Order (NLO) event generator. It models events at parton level using Monte Carlo (MC) simulations. Matrix elements can be calculated for any user-defined Lagrangian using the MADGRAPH framework. A leading order implementation of the SMEFT for MADGRAPH has been done in the *dim6top* [42] model. In this model, all the dimension six SMEFT operators involving a top quark are included. The details of this model are explained in Section 2.2.3. The *dim6top* model was imported into MADGRAPH for generating the SMEFT samples.

As explained in Section 2.2.3, three operators are relevant for the $t\bar{t}\gamma$ production. These operators are added to the SM Lagrangian with a dimensionless Wilson coefficient. The main aim of this thesis is to extract limits on these Wilson coefficients. The $t\bar{t}\gamma$ process, explained in Section 2.1.2, is ideal for extracting these limits as it includes events where a photon is radiated directly from the top quark.

Generating the NLO samples for the $t\bar{t}\gamma$ process, including the full decay of the top quarks is computationally intensive and cannot be completed within the time frame of this analysis. Hence, in this analysis, LO samples will be used. Also, only one of the decay channels is considered. To reduce the computational time further, the first set of studies is done on $pp \rightarrow t\bar{t}\gamma$ samples, without including the decay of the top quark. This is done to get a general idea on the nature of the events, as well as identify a reasonable range of values for each of the Wilson coefficients. For this first set of studies, a range of values for the Wilson coefficients are chosen based on some previous measurements [52].

Samples are generated by varying one of the EFT operators and keeping the other two at zero. Ten values were chosen for each of the Wilson coefficient within the existing limits for generating these samples. The cross-section values for each of these points were plotted. With

Wilson Coefficient	Limits from previous analysis	Value Chosen	
		Negative	Positive
C_{tW}	[-2.0, 1.0]	-1.2	1.0
C_{tZ}	[-6.3, 7.4]	-1.0	1.4
C_{tG}	[-0.4, 0.4]	-0.4	0.4

Table 4.1.: Existing limits on the Wilson coefficients and the values chosen for sample generation [52].

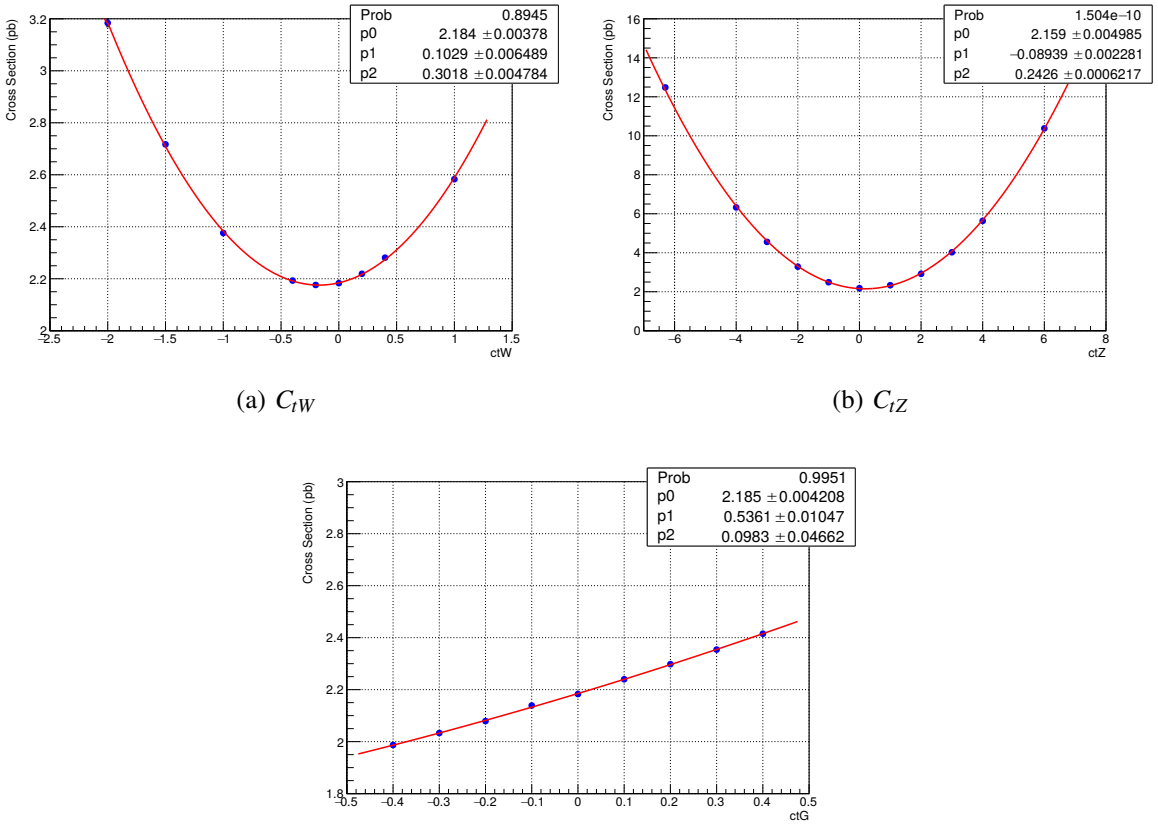

(a) C_{tW} (b) C_{tZ}

(c) C_{tG}

Figure 4.1.: Cross-section as a function of the Wilson coefficients. A second order polynomial of the form $p_0 + p_1 C + p_2 C^2$ is fitted to the simulated points.

the assumption that the cross-section can be expressed as a second-order polynomial function of the Wilson coefficients, such a function is fit to the cross-section plot. These plots are shown in Fig. 4.1.

The following concept is used to pick a value of the Wilson coefficient for generating the $t\bar{t}\gamma$ sample, including the full decay of the top quark. The cross-section value corresponding to a 10% deviation from the SM cross-section is calculated. This reflects the assumed order of uncertainty in the $t\bar{t}\gamma$ cross-section measurement [53]. This value of the cross-section is substituted into the fit function and the two roots of the polynomial function are extracted. These two values (a positive and a negative value) are used for generating the next set of samples. These values are summarised in Table 4.1. Further, to study the differential cross-section, distributions of photon p_{T}, photon $|\eta|$ and $\Delta R_{min}(t,\gamma)$ were also made for these samples as seen in Fig. 4.2. These distributions are normalised to the cross-section times luminosity to obtain the differential cross-section. Some interesting trends can be observed in these plots, which will help to extract better limits on the Wilson coefficients. For example: In the $\Delta R_{min}(t,\gamma)$ distribution, there is a difference in the nature of the distribution (a small bump around π) when compared to the SM sample. Also for the photon p_{T} distribution, the number of events with

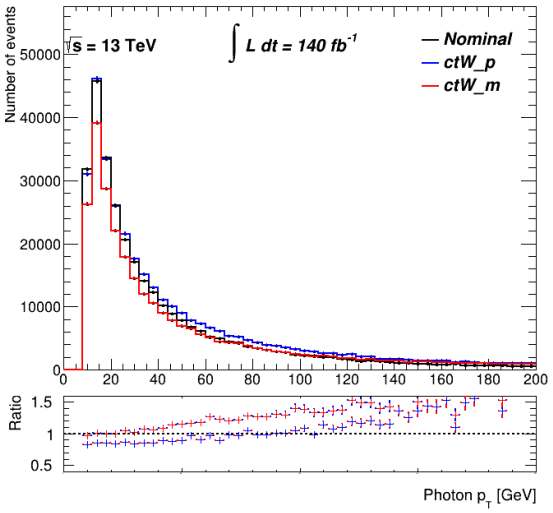

(a) Photon p_{T}

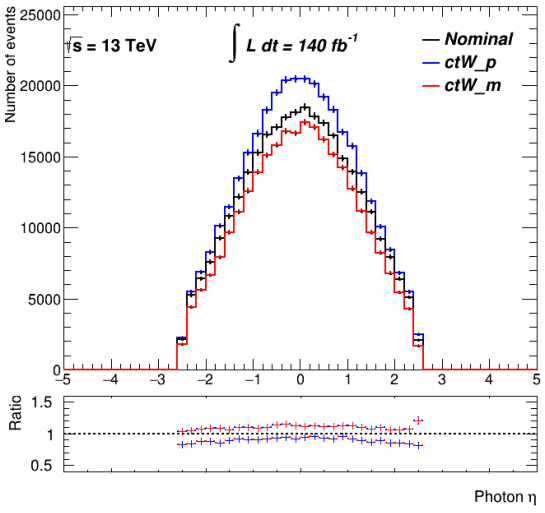

(b) Photon $|\eta|$

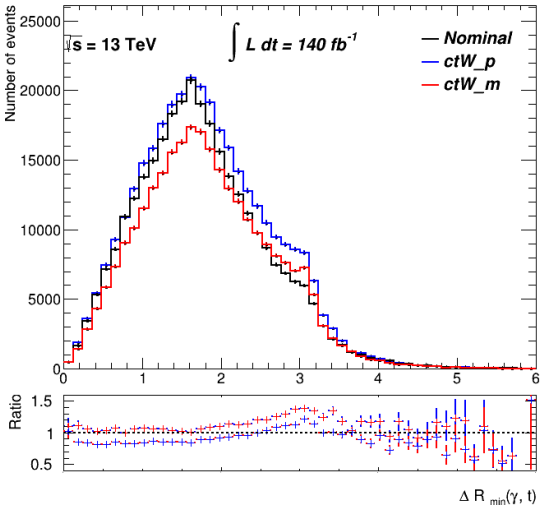

(c) $\Delta R_{min}(\gamma, t)$

Figure 4.2.: Differential cross-section for a positive and negative addition of the O_{tW} operator is compared to the SM. Here, the black line corresponds to the SM like sample, blue corresponds to the sample with a positive (1.0) and red corresponds to the negative (-1.2) addition of the operator.

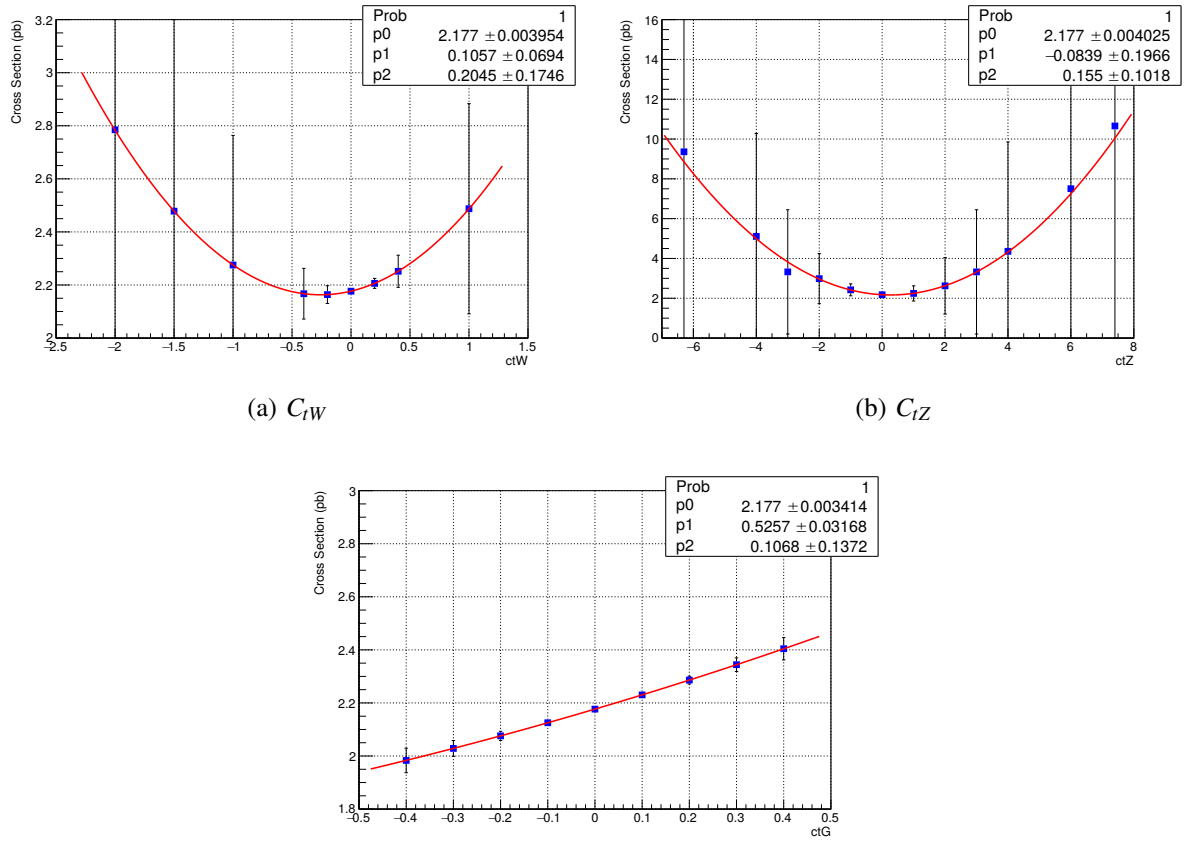

(a) C_{tW}

(b) C_{tZ}

(c) C_{tG}

Figure 4.3.: Cross-section as a function of Wilson coefficient for the samples generated using the reweighting tool.

higher p_{T} are higher for the EFT samples.

4.1. Reweighting tool

Since generating the EFT samples is computationally intensive and time-consuming, an attempt was done to use a reweighting tool to generate multiple samples simultaneously. Using this method, an SM event is generated and for each value of the Wilson coefficient, the probability for this event to occur is calculated and stored as an event weight.

To test the validity of the reweighting tool, as a first step, $pp \rightarrow t\bar{t}\gamma$ samples were generated for the ten different Wilson coefficient values that were used previously, and the cross-section was plotted as a function of the Wilson coefficient as before, and is shown in Fig. 4.3. It was observed that for larger values of the Wilson coefficient, the uncertainty in the cross-section measurement is very high.

To further identify how these uncertainties affect the differential cross-section measurements, distributions of some of the kinematic variables like photon $|\eta|$ and $\Delta R_{min}(t,\gamma)$ were plotted. For some values of the observable, large uncertainties were observed. An example is shown

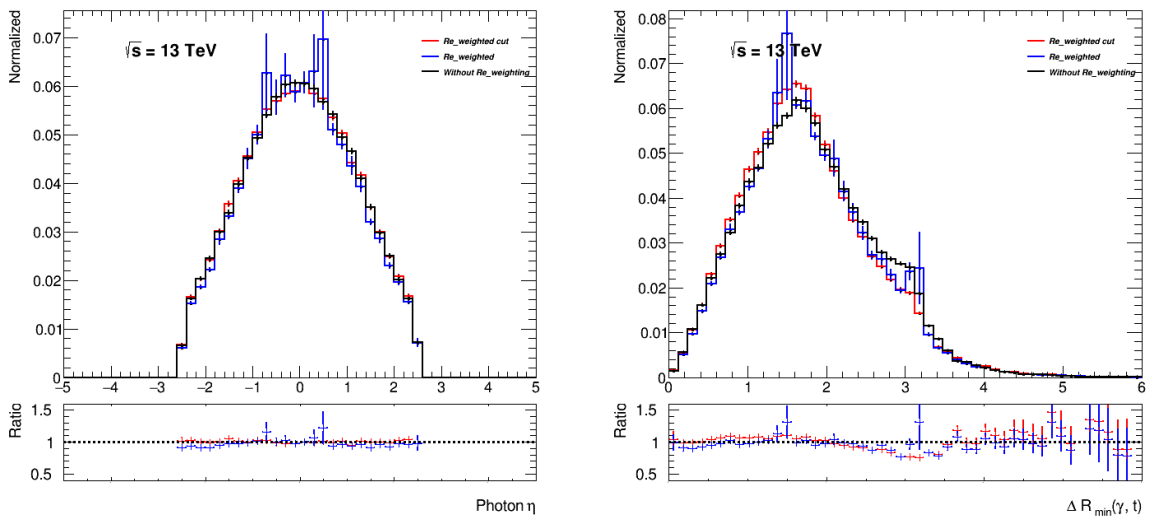

(a) Photon η (b) $\Delta R_{min}(\gamma,t)$

Figure 4.4.: For a positive addition of the O_{tW} operator with the Wilson coefficient value of 1.0, the distributions are normalised to 1. The blue line represents the reweighted sample, and the red line represents the reweighted sample including only the events with a weight lower than 10.

in Fig. 4.4. This observation is because some of the events are scaled by very large weights, which leads to high uncertainties in these bins. This means that there are a few events in the SM which are expected to be observed much more frequently in the EFT model. As mentioned in the documentation for the reweighting tool[1], the events with a weight higher than ten can lead to large statistical uncertainties, and in case these are very few they can be dropped. An attempt was made to remove these events by placing a cut on the weights. In this case, it was observed that the large error bars vanish. But along with that, the interesting features in the distribution mentioned previously also vanish. Also, the ratio between the red (reweighted sample after applying a cut on events with weights higher than 10) and black (non-reweighted sample) distributions in Fig. 4.4 is not unity. Hence, applying a cut on the weights is not an ideal solution. Therefore, the reweighting tool was not used for generating the sample.

4.2. Generating a $t\bar{t}\gamma$ sample in the $e\mu$ final state

An inclusive and differential cross-section measurement of the $t\bar{t}\gamma$ process with the full LHC Run2 data corresponding to an integrated luminosity of 139 fb^{-1} has been done recently [53]. The differential cross-sections measured have been unfolded to parton level. Therefore these measurements can be used directly to extract limits on the Wilson coefficients. The final sample sets for this analysis have been generated using the same event selections and object definitions

[1] https://twiki.cern.ch/twiki/bin/viewauth/AtlasProtected/MadGraph5aMCatNLOreweight

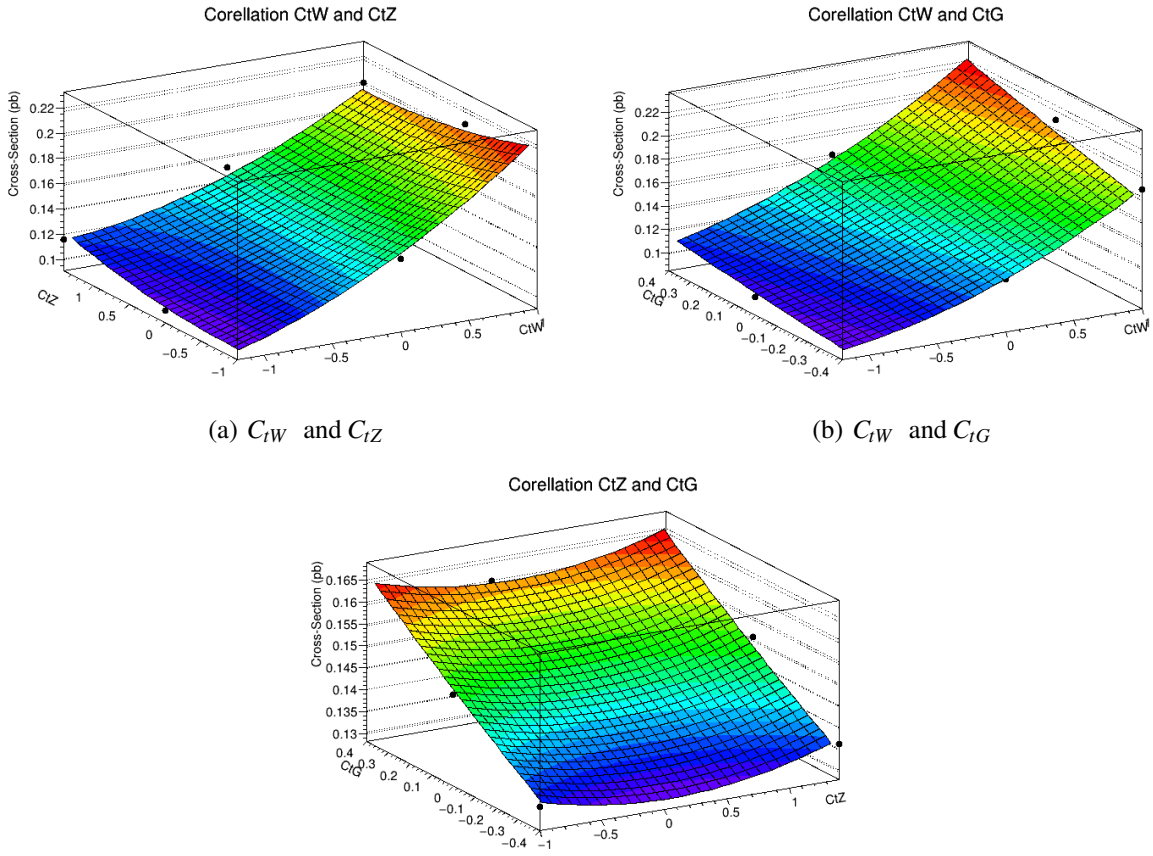

(a) C_{tW} and C_{tZ}

(b) C_{tW} and C_{tG}

(c) C_{tZ} and C_{tG}

Figure 4.5.: Cross-section as a function of two Wilson coefficients simultaneously.

as done in that analysis. Only events in the $e\mu$ final state have been generated, i.e; events where both the top quarks decay into two different leptons. The events where the top quark decays into tau leptons is considered as background. The two processes studied in this analysis are:

$$\begin{aligned} pp \to t\bar{t}\gamma \to e^+\mu^-\nu_e\bar{\nu}_\mu b\bar{b}\gamma \\ pp \to t\bar{t}\gamma \to e^-\mu^+\nu_\mu\bar{\nu}_e b\bar{b}\gamma \end{aligned} \tag{4.1}$$

As discussed in section 2.2.3, there are three relevant EFT operators. It is not necessary that only one of these operators are present in the Lagrangian. The effects observed in nature could be a combination of some or all of these operators. Also, these operators could have some correlation with each other. To check for such effects, events were generated by varying two operators simultaneously and keeping the contribution from the other operator as zero. The 3-D plots with cross-section as a function of two Wilson coefficients can be seen in fig 4.5. These points were then fit to a two-dimensional second-order polynomial. The fit functions are given below in Eq. 4.2. All the three operators clearly show some correlation, as the coefficients of the cross terms are non zero.

$$\begin{aligned}
\sigma(C_{tW},C_{tZ}) &= 0.1444 + 5.2534\times10^{-2}C_{tW} - 2.7931\times10^{-3}C_{tZ} - 8.4904\times10^{-3}C_{tW}C_{tZ} \\
&\quad + 1.2846\times10^{-2}C_{tW}^2 + 3.8096\times10^{-3}C_{tZ}^2 \\
\sigma(C_{tW},C_{tG}) &= 0.1444 + 5.1401\times10^{-2}C_{tW} + 4.1026\times10^{-2}C_{tG} + 1.2674\times10^{-2}C_{tW}C_{tG} \\
&\quad + 1.2577\times10^{-2}C_{tW}^2 + 4.8875\times10^{-3}C_{tG}^2 \\
\sigma(C_{tG},C_{tZ}) &= 0.1444 - 9.0435\times10^{-4}C_{tZ} + 3.9255\times10^{-2}C_{tG} - 7.9456\times10^{-4}C_{tZ}C_{tG} \\
&\quad + 3.909\times10^{-3}C_{tZ}^2 + 4.4026\times10^{-3}C_{tG}^2
\end{aligned} \tag{4.2}$$

Hence, effects due to all the three EFT operators have to be studied simultaneously. For this, a positive, a negative and zero contribution is considered for each of the operators. This gives a total of 27 possible combinations which are listed in table 5.1.

5. Extracting limits on Wilson coefficients

As discussed above, 27 sample sets of the $t\bar{t}\gamma$ process with different EFT parameters were generated in the $e\mu$ final state. As mentioned in Section 4.2, the limits in this analysis are extracted using the results from a recent cross-section measurement of the $t\bar{t}\gamma$ process. To match the fiducial phase space on which the measurement was done to the one used in this analysis, the following selection cuts were made on the samples:

- Every event must have exactly one electron and one muon
- Two b quarks
- Leptons: $p_T > 25$ GeV and $|\eta| < 2.5$
- Photons: $E_T > 20$ GeV and $|\eta| < 2.37$
- b quarks: $p_T > 25$ GeV and $|\eta| < 2.5$
- $\Delta R(\ell,\gamma) > 0.4$, $\Delta R(e,\mu) > 0.4$, $\Delta R(b,\bar{b}) > 0.4$, $\Delta R(\ell,b) > 0.4$

5.1. Obtaining the EFT parameterization equation

After applying the selection cuts on the sample, the selection efficiency was calculated by taking the ratio of the number of events that pass the selection criteria and the total number of events. Further, to make the cross-section comparable to the measurement, the fiducial cross-section value was computed. This was done by taking the product of the cross-section and the selection efficiency for each of the samples. These fiducial cross-section values were fit to a general second-order function of the form shown below and the fit parameters were extracted.

$$\begin{aligned}\sigma = \sigma_{SM} + aC_{tW} + bC_{tZ} + cC_{tG} + dC_{tW}^2 + eC_{tZ}^2 \\ + fC_{tG}^2 + gC_{tW}C_{tZ} + hC_{tZ}C_{tG} + iC_{tW}C_{tG}\end{aligned} \tag{5.1}$$

Here, a,b,c,d,e,f,g,h and i are the fit parameters and σ_{SM} is the Standard Model LO cross-section value. The validation of this fit is done by calculating the ratio of the fiducial cross-section and the value of the fit function, as shown in Table 5.1. This fitted function gives the parametrisation over the full phase space formed by the three Wilson coefficients. The parametrised equation obtained after the fit is given by:

C_{tW}	C_{tZ}	C_{tG}	Fiducial cross-section (fb)	Fit Value	Ratio	C_{tW}	C_{tZ}	C_{tG}	Fiducial cross-section (fb)	Fit Value	Ratio
0	0	0	27.01 ± 0.06	27.01	1.00	M	0	P	22.82 ± 0.03	22.57	0.99
0	0	P	29.93 ± 0.04	30.67	1.02	P	P	0	36.38 ± 0.05	36.92	1.02
0	0	M	24.49 ± 0.04	23.90	0.98	M	P	0	27.89 ± 0.05	28.72	1.03
0	P	0	29.54 ± 0.04	28.78	0.97	P	M	0	49.42 ± 0.06	47.96	0.97
0	M	0	29.44 ± 0.04	30.29	1.03	M	M	0	18.99 ± 0.03	18.80	0.99
P	0	0	40.23 ± 0.06	40.71	1.01	0	P	M	27.36 ± 0.04	25.96	0.95
M	0	0	20.78 ± 0.03	20.28	0.98	P	P	M	32.73 ± 0.05	32.96	1.01
0	P	P	33.37 ± 0.06	32.14	0.96	M	P	M	25.14 ± 0.05	27.29	1.09
0	M	P	33.13 ± 0.06	34.16	1.03	P	0	M	35.76 ± 0.06	36.46	1.02
P	P	P	40.63 ± 0.05	41.44	1.02	M	0	M	18.65 ± 0.03	18.56	0.99
P	M	P	56.59 ± 0.07	52.98	0.94	P	M	M	43.15 ± 0.06	43.50	1.01
M	P	P	31.04 ± 0.05	30.71	0.99	0	M	M	26.41 ± 0.04	26.97	1.02
M	M	P	20.99 ± 0.03	21.29	1.01	M	M	M	17.08 ± 0.03	16.86	0.99
P	0	P	45.21 ± 0.06	45.52	1.01						

Table 5.1.: Fit Validation: The fiducial cross-section value is fitted to Equation 5.1, and values of the fit parameters are extracted. The ratio of Equation 5.2 to the fiducial cross-section is calculated to validate the fit. Here P corresponds to the positive value and M corresponds to the negative value in Table 4.1

$$\begin{aligned}\sigma =& 27.01 + 10.02\, C_{tW} - 1.39\, C_{tZ} + 8.46\, C_{tG} + 3.68\, C_{tW}^2 + 1.89\, C_{tZ}^2 \\ &+ 1.72\, C_{tG}^2 - 3.97\, C_{tW} C_{tZ} + -0.52\, C_{tZ} C_{tG} + 2.87\, C_{tW} C_{tG}\end{aligned} \tag{5.2}$$

It was observed that the predicted SM LO cross-section varies from the measured value by about 25%, but the NLO cross-section is within the limits of the uncertainty of the measurement. All the studies in this analysis are done at LO and to make it comparable to the measurement, the fit functions are shifted by a constant value. The shift was done in a way that when all the Wilson coefficients are set to zero, the function returns the SM NLO cross-section [54] instead of the LO cross-section. This is done with the assumption that there are no additional effects at NLO on the cross-section due to the EFT operators, other than a linear scaling. Also, this scaling for all the EFT samples is considered to be same as the scaling for the SM sample.

5.1.1. EFT parametrisation from differential cross-section

Limits on three EFT parameters cannot be derived using just one parametrized equation. Also, better limits on the Wilson coefficients can be obtained using the differential cross-section, as it includes much more information. Hence, for each of these samples, the differential cross-section as a function of photon p_{T}, photon η, $\Delta R_{min}(\gamma,\ell)$, $\Delta\phi(\ell,\ell)$ and $\Delta\eta(\ell,\ell)$ are also determined. For this, the distribution of each of these observables are plotted and then normalised to the product of fiducial cross-section times the luminosity. This gives the cross-section for each

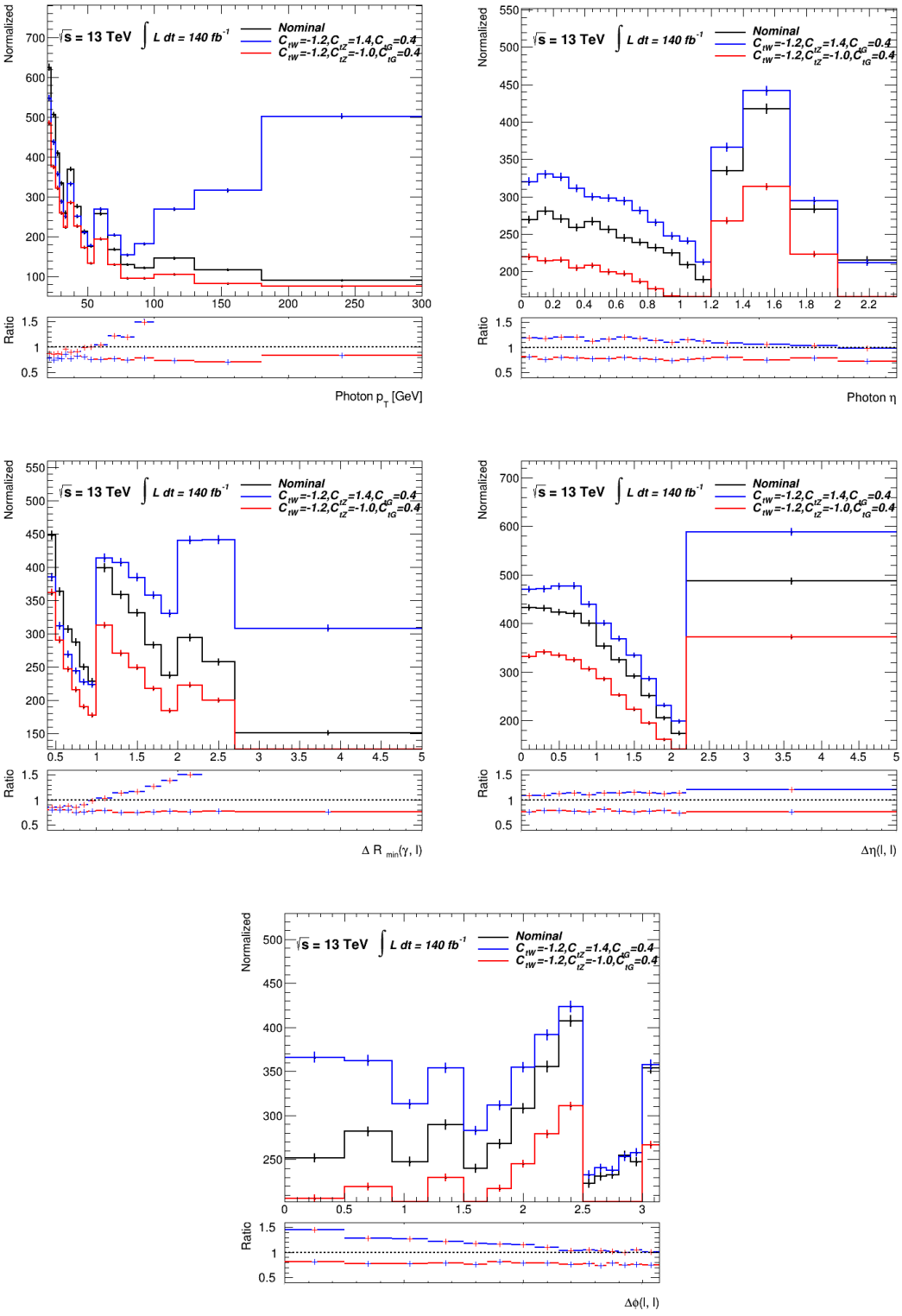

Figure 5.1.: Differential cross-section with respect (a)photon p_{T}, (b) photon $|\eta|$, (c) $\Delta R_{min}(\gamma,\ell)$, (d) $\Delta\phi(\ell,\ell)$ and (e) $\Delta\eta(\ell,\ell)$. Here the black line represents the SM like sample. The blue line and red line are two samples with non zero contribution from multiple EFT operators. These distributions are normalised to the product of cross-section times the luminosity.

bin. The binning for each of these distributions is adapted from the recent $t\bar{t}\gamma$ cross-section measurements so that a comparison can be made. An example of these plots for three of the samples overlayed can be seen in Fig. 5.1. Here, the blue line corresponds to the EFT sample with C_{tW} = -1.2, C_{tZ} = 1.4 and C_{tG} = 0.4, and the red line corresponds to C_{tW} = -1.2, C_{tZ} = -1.0 and C_{tG} = 0.4. These two samples are compared with the black line, which represents the SM sample.

To extract EFT parametrisation from these differential cross-section plots, for each bin, the cross-section values from all the 27 samples are obtained and fit to a second-order polynomial, in the same manner as it was done for the inclusive cross-section values. This is done for all the bins and for all the five observables. Similar to the fit function for the fiducial cross-section, all the fit functions are shifted by a constant value to match the NLO SM cross-section to obtain the final EFT parametrisation equations mentioned in Appendix A.

Testing the fit

To check the accuracy of the fit, these fit functions are tested by calculating the relative deviation from the cross-section as per the following equation.

$$\text{Relative deviation} = \frac{F(C_{tW}, C_{tZ}, C_{tG}) - \text{Bin content}}{\text{Bin content}} \tag{5.3}$$

Here, the bin content is the actual cross-section value obtained in each bin from the simulated samples. For a good fit, the relative deviation would be very close to zero. For a distribution with n bins, there will be n fit functions. Each of these functions are obtained by fitting 27 points. Hence, for each observable, there are n fit functions and $27n$ values of relative deviation.

The distributions of these relative deviations are shown in Fig. 5.2. As expected, it peaks at zero, but there are a few points for which the relative deviation value is not close to zero and are as high as 10%. Since the deviation from the fit is quite high for some points, these deviations cannot be ignored,e and the fit cannot be considered ideal. Hence, these deviations are added as an additional uncertainly while extracting the limits.

5.2. EFT*fitter* tool

The EFT*fitter* tool [55] is used to extract limits on the Wilson coefficients. This tool is developed using the *Bayesian Analysis Toolkit* (BAT) [56], which is based on the Bayes Theorem and is implemented using the Markov Chain Monte Carlo method. In this section, working of BAT is explained to understand the background of the EFT*fitter* tool. Further, it also explains how to use the tool and validate it.

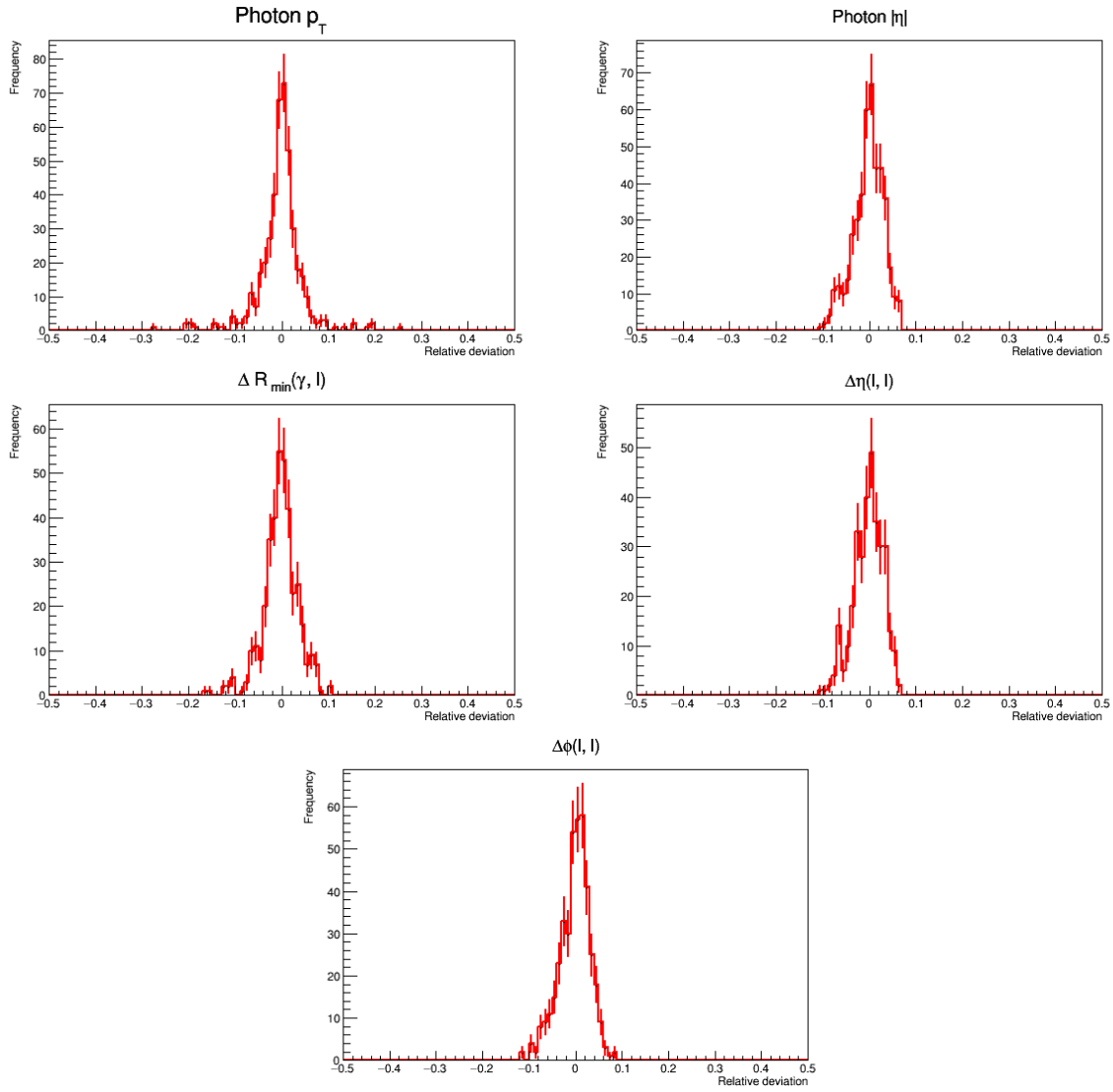

Figure 5.2.: The relative deviation of all the 27 points from the fit function is plotted for all the bins in a distribution. (a) photon p_{T}, (b) photon η, (c) $\Delta R_{min}(\gamma,\ell)$, (d) $\Delta\phi(\ell,\ell)$ and (e) $\Delta\eta(\ell,\ell)$

5.2.1. Working of BAT

The main aim of BAT is to compare model predictions with data to validate the model or predict the values of the parameters in the model. This can be done by comparing data ($\vec{D}$) with the model. Consider a model M, with parameters $\vec{\lambda}$, the function $g(\vec{y}|\vec{\lambda},M)$, gives the relative frequency of getting the result $\vec{y}$ from this model. This function should also satisfy:

$$g(\vec{y}|\vec{\lambda},M) \geq 0 \text{ and } \int g(\vec{y}|\vec{\lambda},M)d\vec{y} = 1. \tag{5.4}$$

But this function cannot be directly compared to data as the data includes effects from the experimental setup. These effects can be either included in the model as additional (nuisance) parameters or removed from the data by using methods like unfolding. In this analysis, the detector effects on data have been removed using the unfolding procedure, and hence these

nuisance parameters do not need to be considered in the model.

The probability of obtaining a particular value of $\vec{\lambda}$ is given by $P(\vec{\lambda}|M)$. This probability can be obtained as per the Bayes theorem as follows:

$$P_{i+1}(\vec{\lambda},M|\vec{D}) = \frac{P(\vec{D}|\vec{\lambda},M)P_i(\vec{\lambda},M)}{P(\vec{D})}. \tag{5.5}$$

$P_i(\vec{\lambda},M)$ is the prior, which is some initial information about the parameters. It also defines the range of values the parameter can take. The term, $P(\vec{D}|\vec{\lambda},M)$, is the likelihood function, which must be defined for all possible values data can take. It is defined using the model and includes the information about the detector setup. In this analysis, these are obtained from the fit functions that are extracted from the differential cross-sections. Using this information, $P_{i+1}(\vec{\lambda},M|\vec{D})$ is calculated, which is the posterior probability density function (*pdf*). The posterior *pdf* is computed iteratively over the variable i with the Markov Chain to optimise the results.

The posterior *pdf* contains a lot of information and can be used to extract details like mean, mode, median, marginalized *pdf*, correlations between parameters, central interval and smallest interval. The smallest interval containing α of the probability is given by $[P(\vec{\lambda}^*|\vec{D},M),\ P_{min}]$ which can be calculated from the following relation:

$$\alpha = \int_{P_{min}}^{P(\vec{\lambda}^*|\vec{D},M)} p(P(\vec{\lambda}|\vec{D},M))dP(\vec{\lambda}|\vec{D},M) \tag{5.6}$$

Here, $p(P(\vec{\lambda}|\vec{D},M))$ is the probability density of the posterior *pdf*. A numerical implementation of this is done in BAT using the Markov Chain Monte Carlo method.

5.2.2. Using EFT*fitter*

EFT*fitter* is a tool that calculates the posterior probabilities of the free parameters in EFT, using BAT. For calculating the probabilities, the tool requires the following as input:

- A description of the model in terms of the free parameters and measured observables. These are given by the polynomial fit function mentioned in appendix A.
- The measured value of the observables (data) and the values of different types of measurement uncertainties.
- Correlation matrix between the observables for each type of uncertainty.

Validation of EFT*fitter*

The EFT*fitter* tool has to be validated before using it for extracting the limits on the Wilson coefficients. For this, values of cross-section corresponding to know values of Wilson coefficients are given as the measured value (pseudo data). The posterior probabilities are calculated

Sample	Wilson Coefficient	Expected value	Global Fit value
SM	C_{tW}	0	-0.009 ± 3.90
	C_{tZ}	0	-0.007 ± 3.34
	C_{tG}	0	0.0106 ± 7.13
Non-SM	C_{tW}	0	-0.101 ± 0.66
	C_{tZ}	-1	-0.997 ± 1.10
	C_{tG}	0.4	0.479 ± 0.69

Table 5.2.: Closure test results for a SM-like and a non-SM-like points. The uncertainties on the global fit value are the expected allowed 1σ ranges.

for the Wilson coefficients using EFT*fitter*. The global fit value for the Wilson coefficients are compared to the expected value.

As a first test, the SM NLO differential cross-section with respect to photon p_{T} is used as the pseudo data. The systematic and statistical uncertainty from the measurement is combined and added as an uncertainty. The deviation from the EFT parametrisation function obtained in Fig. 5.2 is added as another uncertainty. The EFT parametrisation equations obtained from the differential cross-section as a function of photon p_{T} is used as the model description (listed in Appendix A). Using these, the posterior probabilities were calculated for the three Wilson coefficients.

The one dimensional and two dimensional marginalized distributions are shown in Fig. 5.3. The global fit value for all the three Wilson coefficients is very close to zero as expected. Similarly, the test was done for all the five observables, ie; photon p_{T}, photon $|\eta|$, $\Delta R_{min}(\gamma,\ell)$, $\Delta\phi(\ell,\ell)$ and $\Delta\eta(\ell,\ell)$ and the results obtained were very close to zero just like the results obtained for Photon p_{T}.

Such validation tests were also done on the non-SM like points. For this, one of the non-SM sample points is chosen. The difference between the LO and the NLO SM cross-section was added to the LO cross-section of this point, to obtain the pseudo data. This value now corresponds to the NLO cross-section for this point as per our assumption and can be compared to the shifted fit function. Using this value as the pseudo data, posterior probabilities are calculated, and the marginalized distributions are plotted. For example, in Fig. 5.4 the point C_{tW}= 0, C_{tZ}= -1 and C_{tG}= 0.4 is chosen, and the marginalized posterior probabilities are computed for the differential cross-section as a function of photon p_{T}. As seen from the figure and Table 5.2, the global fit value for the Wilson coefficients is very close to the expected value, proving that the EFT*fitter* tool works as expected.

5.3. Two-dimensional studies

Given that five observables are unfolded to parton level in the latest $t\bar{t}\gamma$ analysis [53], using all this information simultaneously could result in the extraction of the best limits. But as

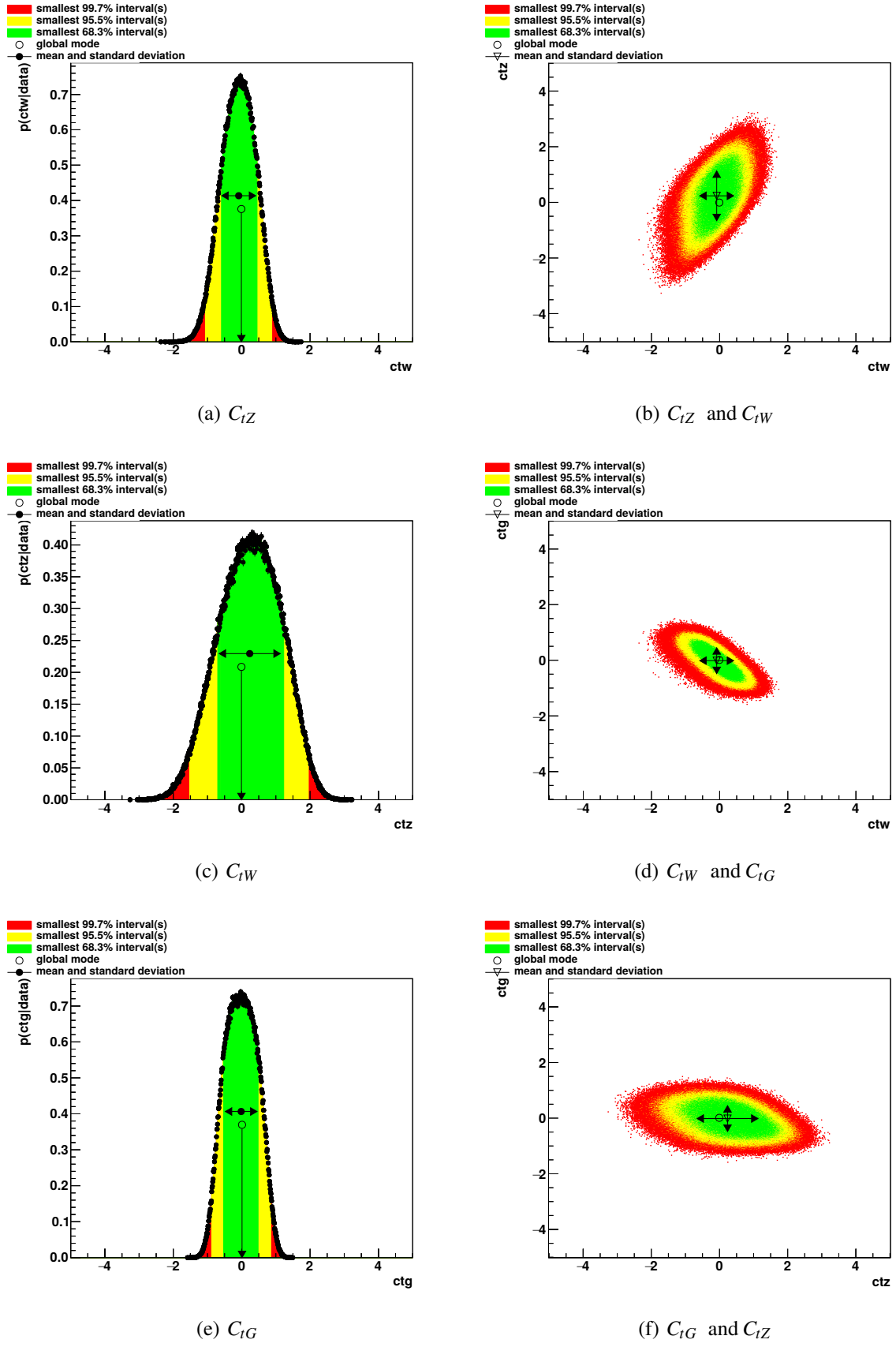

(a) C_{tZ}

(b) C_{tZ} and C_{tW}

(c) C_{tW}

(d) C_{tW} and C_{tG}

(e) C_{tG}

(f) C_{tG} and C_{tZ}

Figure 5.3.: Validation test for SM point for the photon p_{T} observable: One dimensional marginalized distributions for the three Wilson coefficients are on the left. The two dimensional marginalized distributions are shown on the right.

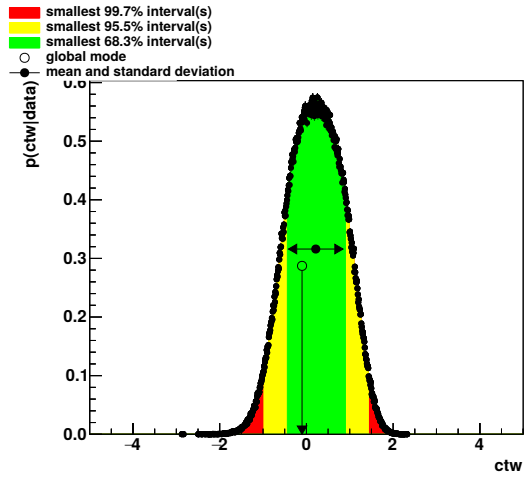

(a) C_{tZ}

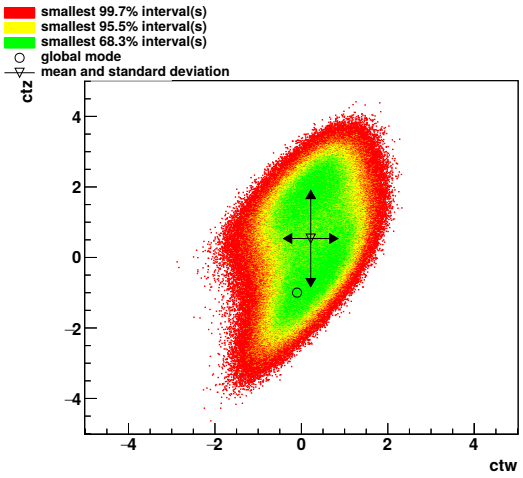

(b) C_{tZ} and C_{tW}

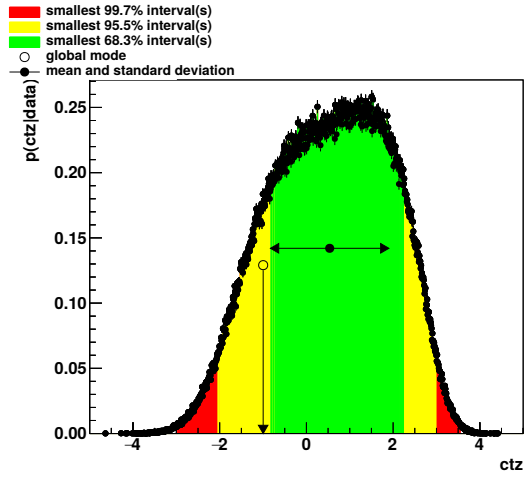

(c) C_{tW}

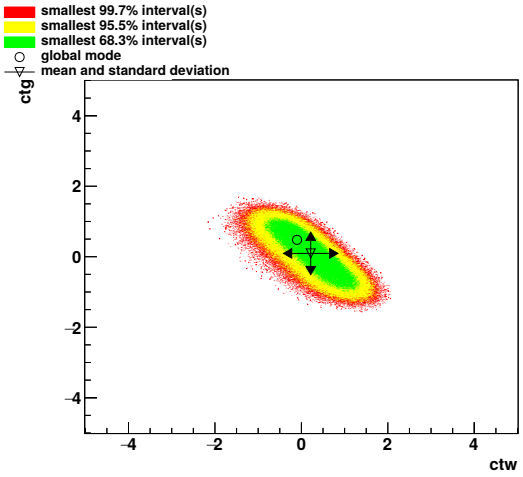

(d) C_{tW} and C_{tG}

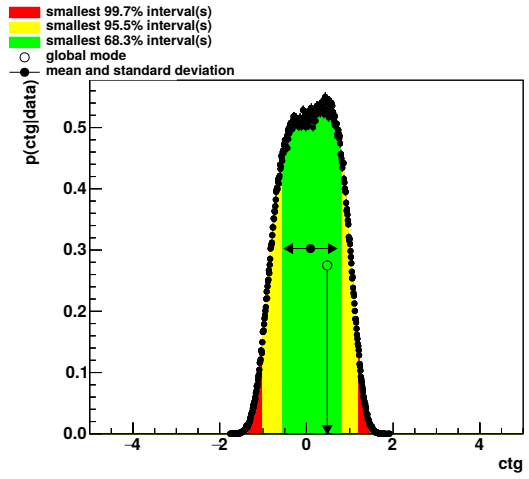

(e) C_{tG}

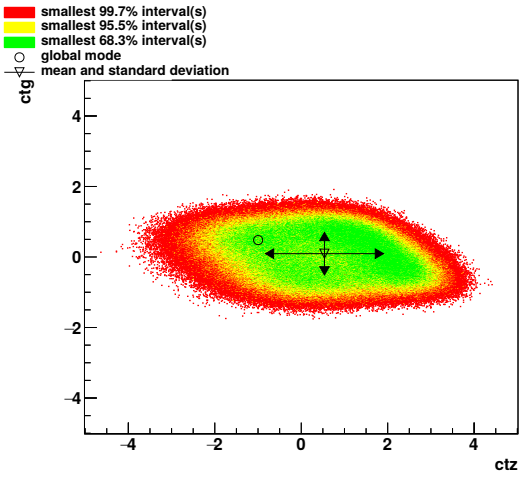

(f) C_{tG} and C_{tZ}

Figure 5.4.: Validation test for non-SM point for the photon p_{T} observable: One and two dimensional marginalized distributions for the point C_{tW} = 0, C_{tZ} = -1, C_{tG} = 0.4.

Sample			Correlation	Sample			Correlation	Sample			Correlation
ctW	ctZ	ctG	factor	ctW	ctZ	ctG	factor	ctW	ctZ	ctG	factor
0	0	0	-0.026	1	1.4	0.4	-0.029	-1.2	-1	0	-0.038
0	0	0.4	-0.035	1	-1	0.4	-0.040	0	1.4	-0.4	-0.052
0	0	-0.4	-0.041	-1.2	1.4	0.4	-0.054	1	1.4	-0.4	-0.025
0	1.4	0	-0.044	-1.2	-1	0.4	-0.032	-1.2	1.4	-0.4	-0.067
(0	-1	0	-0.019	1	0	0.4	-0.046	1	0	-0.4	-0.028
1	0	0	-0.026	-1.2	0	0.4	-0.049	-1.2	0	-0.4	-0.031
-1.2	0	0	-0.041	1	1.4	0	-0.022	1	-1	-0.4	-0.032
0	1.4	0.4	-0.034	-1.2	1.4	0	-0.061	0	-1	-0.4	-0.028
0	-1	0.4	-0.034	1	-1	0	-0.058	-1.2	-1	-0.4	-0.035

Table 5.3.: Correlation factor between Photon p_{T} and Photon $|\eta|$

described in the Subsection 5.2.2, for using two of these observables simultaneously, for each of the uncertainty, the correlation between the different bins of the observables is required. Since in the latest measurement only one dimensional unfolding was done, these correlations have not been computed and are not available.

Nevertheless, some two dimensional studies are done with the assumption that, if the direct correlation between the different bins of the two observables is less than five per cent, it cannot be observed and can be neglected. To check the correlation between pairs of observables, two dimensional differential cross-section plots are made, and the correlation coefficients are calculated. These plots for the SM like samples are shown in Fig. 5.5.

As seen from the plots, the correlation coefficients for most of the combinations are less than 0.05 and can be considered simultaneously to extract limits as per the assumption. To understand how these correlations vary in the presence of the EFT operators, similar plots were made for all the other 26 samples and the correlation factors were calculated. As an example, the correlation between photon p_{T} and photon $|\eta|$ is shown in Table 5.3. As seen from the table, the correlation factors are about 5% for all the sample points. Hence the correlation can be neglected. These correlation factors for all the pairs of operators can be found in Appendix B. From these tables, it was found that for the following pairs of operators, the correlation between them is low and can be ignored:

- Photon p_{T} and photon $|\eta|$
- Photon p_{T} and $\Delta\eta(\ell,\ell)$
- Photon $|\eta|$ and $\Delta R_{min}(\gamma,\ell)$
- Photon $|\eta|$ and $\Delta\eta(\ell,\ell)$
- Photon $|\eta|$ and $\Delta\phi(\ell,\ell)$
- $\Delta\eta(\ell,\ell)$ and $\Delta\phi(\ell,\ell)$

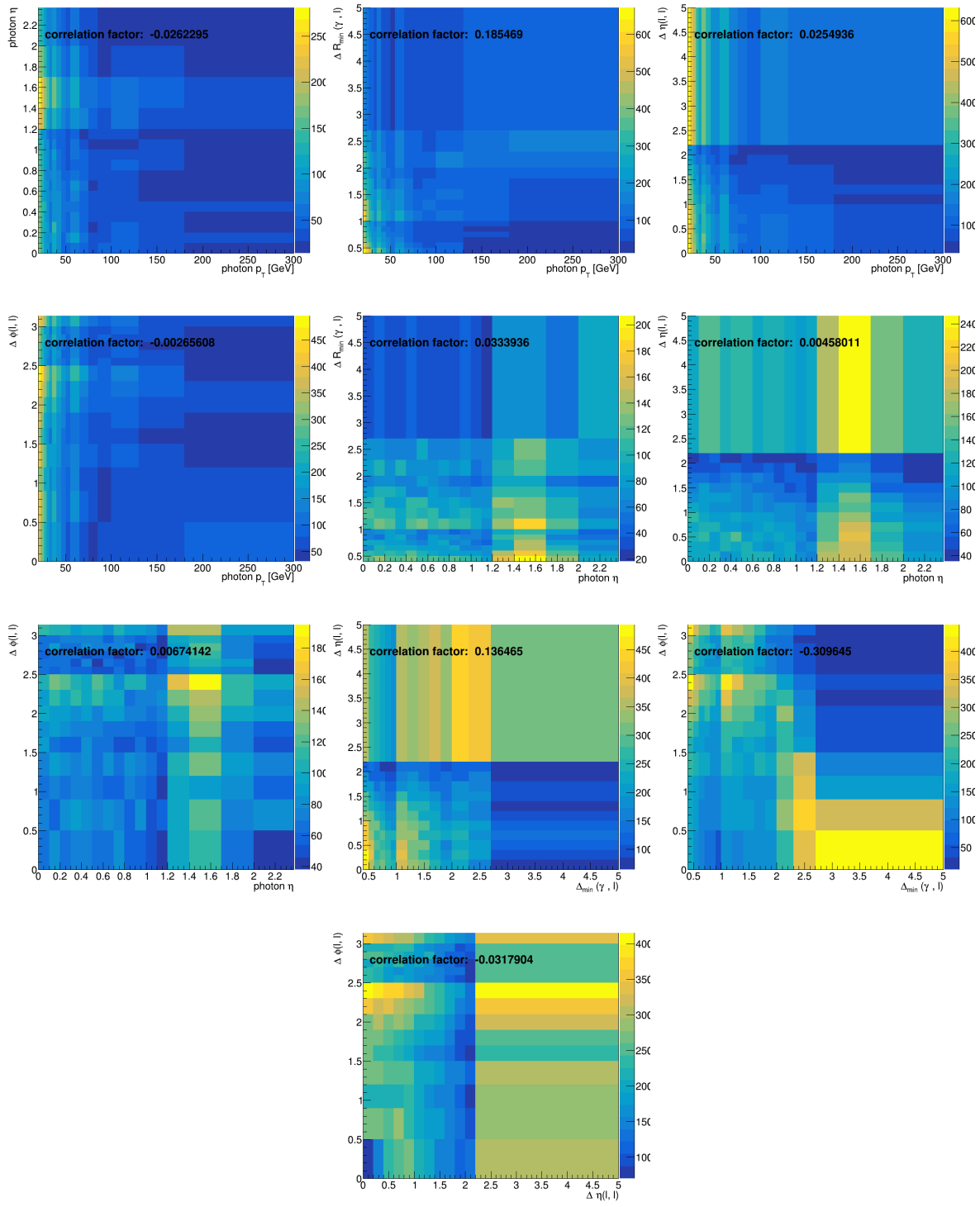

Figure 5.5.: Two dimensional plots with two of the observables on the X and Y axis and the cross-section is denoted by the colour scale. The correlation factor for the pair of observables is mentioned on the plot.

6. Results

Having validated the EFT*fitter* tool, the next step is to extract limits on the Wilson coefficients using the measured cross-section (data). But before doing this, the best observable for extracting the limits has to be identified. Expected limits are calculated by using the SM NLO cross-section as pseudo data for all the five observables. The result of this is summarised in Table 6.1. As observed from the table, the limits with the best constraint are obtained when the p_{T} of the photon is used to extract the limits.

Wilson Coefficient	C_{tW}		C_{tZ}		C_{tG}	
Observable	limit	Width	limit	Width	limit	Width
Photon p_{T}	[-0.59, 0.46]	1.05	[-0.63, 1.22]	1.85	[-0.53, 0.49]	1.02
Photon $\lvert\eta\rvert$	[-1.22, 0.44]	1.66	[-0.75, 1.61]	2.36	[-0.58, 0.53]	1.11
$\Delta R_{min}(\gamma,\ell)$	[-0.67, 0.47]	1.14	[-0.95, 1.34]	2.29	[-0.58, 0.53]	1.11
$\Delta\eta(\ell,\ell)$	[-1.63, 0.55]	2.18	[-0.83, 1.79]	2.62	[-0.71, 0.62]	1.33
$\Delta\phi(\ell,\ell)$	[-0.83, 0.41]	1.24	[-0.79, 1.77]	2.56	[-0.69, 0.45]	1.14

Table 6.1.: 68% confidence level intervals and uncertainties on the Wilson coefficients extracted using one observable.

Wilson Coefficient	C_{tW}		C_{tZ}		C_{tG}	
Observable	limit	Width	limit	Width	limit	Width
Photon p_{T} & photon $\lvert\eta\rvert$	[-0.68, 0.41]	1.09	[-0.72, 1.37]	2.09	[-0.53, 0.50]	1.03
Photon p_{T} & $\Delta\eta(\ell,\ell)$	[-0.71, 0.44]	1.15	[-0.72, 1.43]	2.15	[-0.55, 0.53]	1.08
Photon $\lvert\eta\rvert$ & $\Delta R_{min}(\gamma,\ell)$	[-0.81, 0.44]	1.25	[-0.94, 1.49]	2.43	[-0.61, 0.54]	1.15
Photon $\lvert\eta\rvert$ & $\Delta\eta(\ell,\ell)$	[-1.41, 0.50]	1.91	[-0.89, 1.67]	2.56	[-0.67, 0.58]	1.25
Photon $\lvert\eta\rvert$ & $\Delta\phi(\ell,\ell)$	[-1.05, 0.46]	1.51	[-0.80, 1.73]	2.53	[-0.67, 0.52]	1.19
$\Delta\eta(\ell,\ell)$ & $\Delta\phi(\ell,\ell)$	[-1.13, 0.53]	1.66	[-0.82, 1.84]	2.66	[-0.78, 0.51]	1.29

Table 6.2.: 68% confidence level intervals and uncertainties on the Wilson coefficients extracted using two observables.

As discussed in section 5.3, two observables can also be used simultaneously to extract limits on the Wilson coefficients. Similar to the one dimensional analysis, limits were extracted using NLO SM cross-section values as pseudo-data for all the pairs of observables listed in Section 5.3. These values are shown in Table 6.2. The limits obtained from these combinations are not as strong as the limits obtained using photon p_{T}. This is because, in the two dimensional distribution, the events in one bin of one of the observables get distributed over all the bins of the other observable. Thus, lowering the statistics per bin.

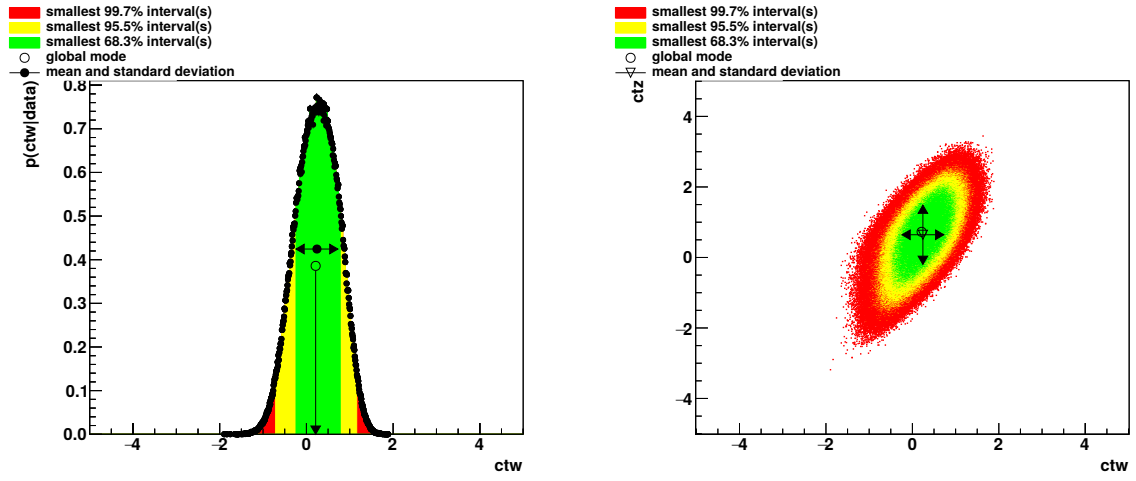

(a) C_{tZ}

(b) C_{tZ} and C_{tW}

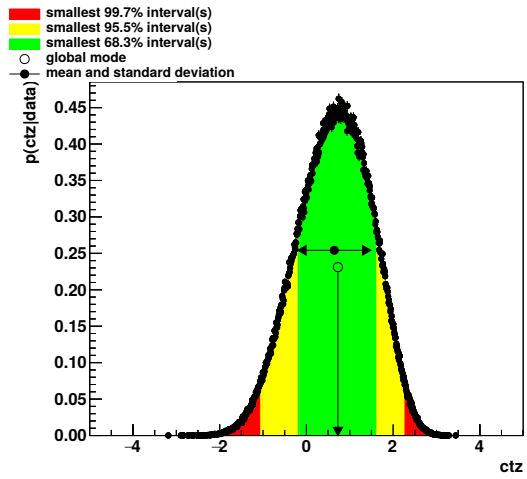

(c) C_{tW}

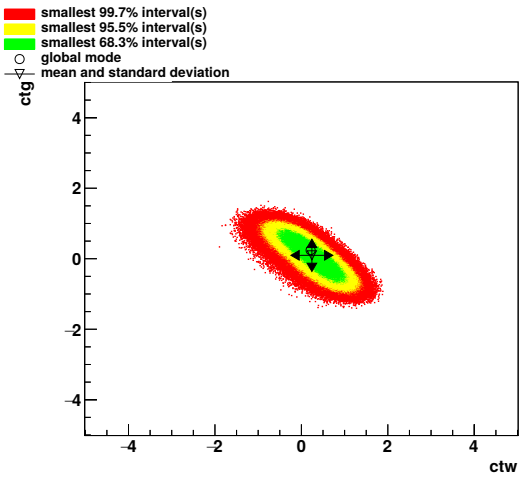

(d) C_{tW} and C_{tG}

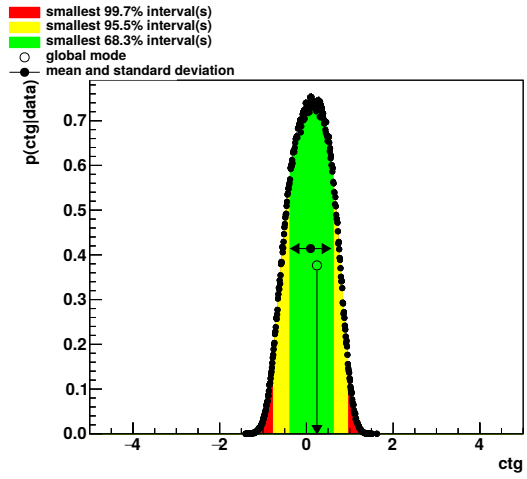

(e) C_{tG}

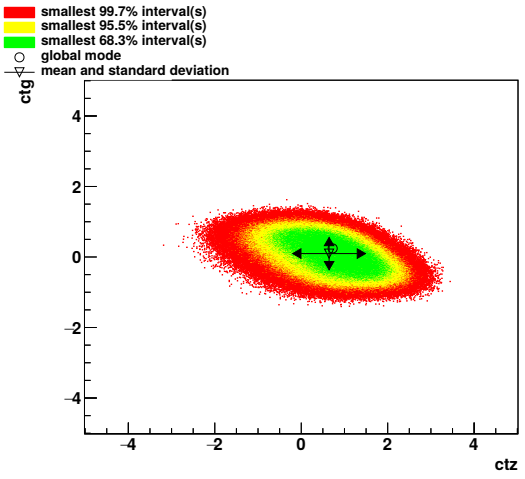

(f) C_{tG} and C_{tZ}

Figure 6.1.: One and two dimensional marginalized distribution of the posterior probabilities for the p_{T} of the photon computed from data.

Posterior probabilities were calculated using EFT*fitter* for the measured photon p_{T} values taken from the cross-section analysis [53] with 139 fb^{-1} of ATLAS data. From these, the smallest interval containing at least 68% probability is identified. These are:

$$C_{tW} \in [\text{-}0.26,\ 0.93] \qquad C_{tZ} \in [\text{-}0.22,\ 2.02] \qquad C_{tG} \in [\text{-}0.42,\ 0.74]$$

These are the best limits that can be extracted from the differential cross-section measurements [53] with an integrated luminosity of 139 fb^{-1}. The one and two dimensional distributions of the marginalised posterior probabilities are shown in Fig. 6.1.

In comparison to previous results [52], especially the limits on C_{tW} and C_{tZ} has improved significantly. This can be explained because this is the first analysis looking into the full ATLAS dataset, which provides more information on differential quantities than previous measurements. In addition, for the first time, the three relevant Wilson coefficients are fitted simultaneously by taking all correlations into account.

7. Conclusion and Outlook

This analysis targeted the coupling between a top quark and a photon and investigated possible BSM effects on this coupling by studying three relevant SMEFT operators. For this, limits were extracted on the three Wilson coefficients associated with these operators. This was done using the differential cross-section measurements with respect to the transverse momentum of the photon produced in the $t\bar{t}\gamma$ process in the $e\mu$ channel. The extracted limits are well within the SM predictions and hence do not show any hint towards BSM contributions to the SM vector coupling of the photon to the top quark.

The limits on these Wilson coefficients could be further improved by increasing the statistics, reducing systematic uncertainties, extracting limits from two dimensional unfolded data or using better models to parametrise the Wilson coefficient phase space. A short study is done on the effect of these changes and is presented in this chapter.

7.0.1. Effect of more data

In general, it is expected that an increase in statistics can help get better constraints on any measurement as the statistical uncertainty would decrease with an increase in the number of events. To understand how much improvement can be expected on the constraints with an integrated luminosity of 500 and 1000 fb^{-1}, the current uncertainties of the measurement were scaled by a factor of $1/\sqrt{n}$. The systematic uncertainties are kept constant. Posterior probabilities were calculated for the SM NLO cross-section and the measured cross-section with the new scaled values of uncertainty. The extracted limits using these new uncertainties are shown in Fig 7.1 and are summarised in Table 7.1

It can be observed that the expected limits are more constrained with an increase in luminosity from 140 fb^{-1} to 500 fb^{-1}. However, on an increase of luminosity from 500 fb^{-1} to 1000 fb^{-1} such an improvement in not observed. This could imply that the analysis is limited mainly by systematic uncertainties in the measurement or other uncertainties like the deviation from the second order polynomial model that was assumed in this analysis.

7.0.2. Effect of reduced systematic uncertainties

From the extrapolation of the statistical uncertainties to higher luminosities, it was observed that there is only a small improvement in the constraints. The cross-section measurement is also associated with systematic uncertainties that originate from measurement uncertainties

Luminosity	With error from the fit				Without error from the fit			
	Expected		From data		Expected		From data	
	Limit	Width	Limit	Width	Limit	Width	Limit	Width
				C_{tW}				
140 fb^{-1}	[-0.74, 0.50]	1.24	[-0.26, 0.93]	1.19	[-0.55, 0.47]	1.02	[-0.21, 0.9]	1.11
500 fb^{-1}	[-0.55, 0.42]	0.97	[-0.17, 0.89]	1.06	[-0.45, 0.41]	0.86	[-0.10, 0.81]	0.91
1000 fb^{-1}	[-0.49, 0.40]	0.89	[-0.16, 0.89]	1.05	[-0.42, 0.39]	0.81	[-0.06, 0.78]	0.84
				C_{tZ}				
140 fb^{-1}	[-0.83, 1.42]	2.25	[-0.20, 1.96]	2.16	[-0.55, 1.08]	1.63	[-0.02, 1.54]	1.56
500 fb^{-1}	[-0.58, 1.26]	1.84	[-0.07, 1.94]	2.01	[-0.43, 1.01]	1.44	[-0.13, 1.38]	1.51
1000 fb^{-1}	[-0.51, 1.16]	1.67	[-0.03, 1.95]	1.98	[-0.43, 0.96]	1.39	[-0.12, 1.31]	1.43
				C_{tG}				
140 fb^{-1}	[-0.59, 0.56]	1.15	[-0.40, 0.71]	1.11	[-0.49, 0.47]	0.96	[-0.69, 0.38]	1.07
500 fb^{-1}	[-0.48, 0.47]	0.95	[-0.32, 0.71]	1.03	[-0.43, 0.42]	0.85	[-0.64, 0.25]	0.89
1000 fb^{-1}	[-0.45, 0.44]	0.89	[-0.32, 0.71]	1.03	[-0.42, 0.40]	0.82	[-0.62, 0.22]	0.84

Table 7.1.: The dependence of the limits on luminosity and uncertainty in the modelling.

due to the resolution of the detector. These can be improved with detector upgrades and better reconstruction techniques.

Another systematic uncertainty in this analysis comes from the model assumed to describe the fiducial cross-section in the Wilson coefficient phase space. The second-order polynomial fit model shows considerably high deviations for some of the EFT samples. A better fit function could be chosen to reduce the uncertainty introduced by this model.

A second order polynomial fit function was chosen as the cross-section can be modelled well using this function as seen in Figure 2.5. But for the fiducial cross-section, some of the points are not modelled precisely by the fit functions as seen in the Section 5.2.2. To understand the effect of this uncertainty on the extracted limits, it was assumed that the the parametrized equations are a perfect model to describe the fiducial cross-section as a function of the Wilson coefficients. In this case, the uncertainties in the model are considered to be zero and the posterior fit functions are computed. From these, the limits on the Wilson coefficients are extracted. These are shown in Fig. 7.2 and summarised in the right half of Table 7.1.

On comparing Fig. 7.2 and Fig. 7.1 it can be seen that there is a only small improvement in the constraints. Hence, the major uncertainty in this analysis is from the systematic uncertainty from the measurement. Even then, an approach that could be taken to avoid this additional uncertainty in the EFT parametrisation by separately fitting the cross-section to a second order polynomial and the selection efficiency to another function and taking a combination of these two functions. This could potentially give a better fit function as observed in another analysis [57].

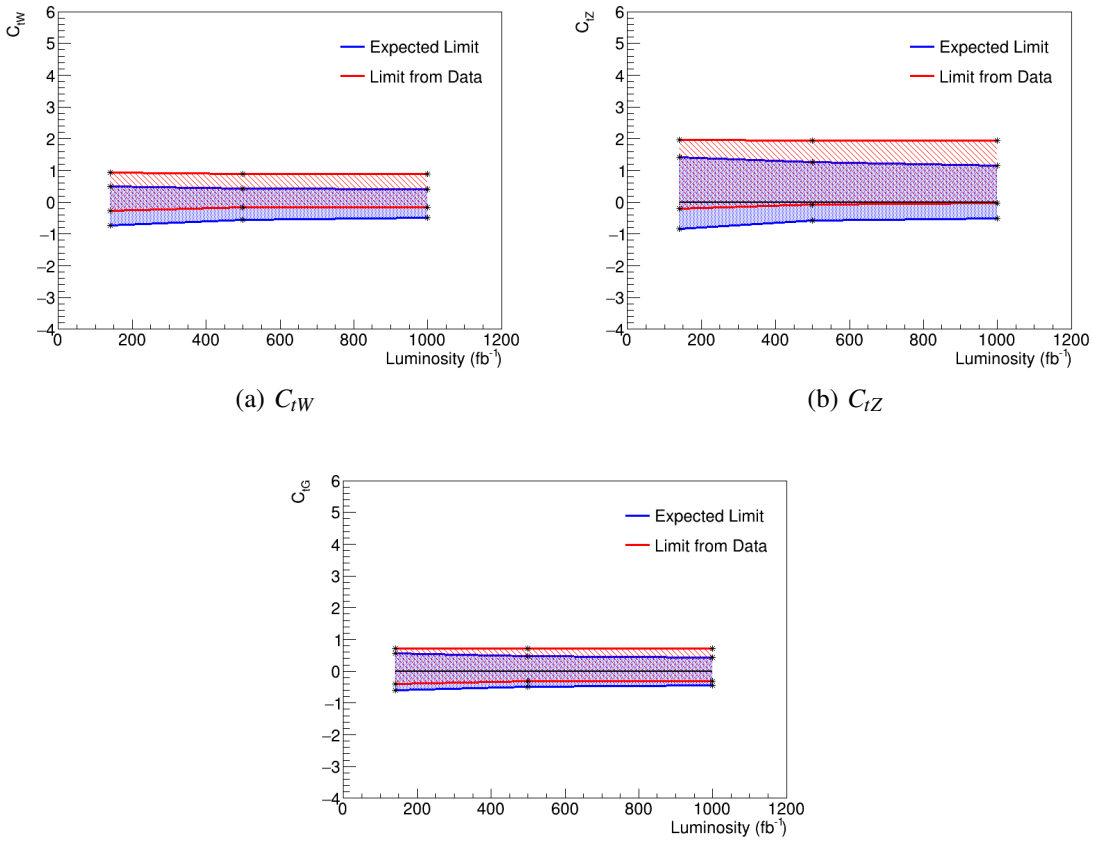

(a) C_{tW}

(b) C_{tZ}

(c) C_{tG}

Figure 7.1.: Dependence of the limits on integrated luminosity

7.0.3. Two dimensional studies

The results from the two dimensional analysis can be improved with additional information like the correlation between the uncertainty in the measurement of these observables. As seen from Table 5.3, there is a small negative correlation between the photon p_{T} and the photon $|\eta|$ observables. This information is not included in this analysis, as two dimensional unfolding has not been done on the differential cross-section measurements, and hence we do not have access to these correlations. Having the correlations, we could also use them to gain extra information, i.e. we could also study the fit result when fitting two variables that have a high correlation. An improvement in the constraints can be expected when limits are extracted with data that also includes this information.

7.0.4. Study of reconstruction effects

This analysis was performed on data that has been unfolded to the parton level. The unfolding procedure takes into account migration effects between reconstructed, and truth level objects and differential selection efficiencies are taken from the SM MC sample. Hence it is also important to check the effect of these on the extracted limits. For this, samples with showering

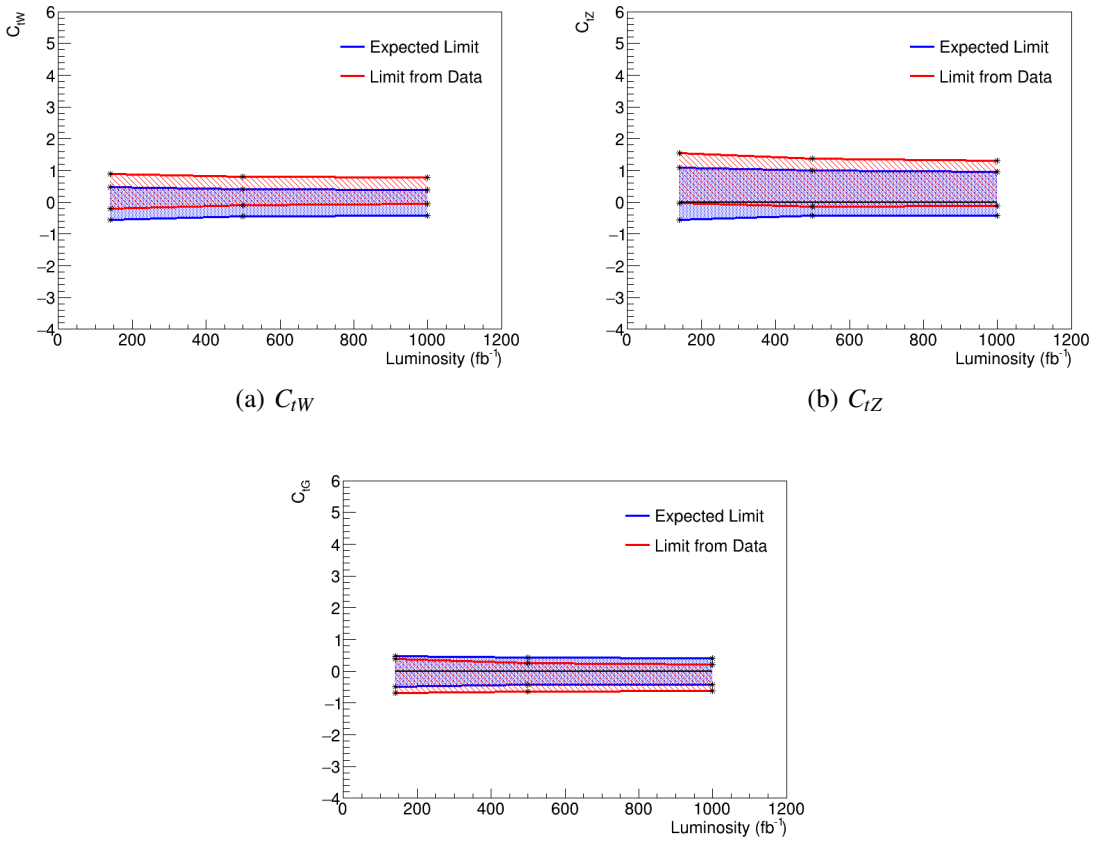

(a) C_{tW}

(b) C_{tZ}

(c) C_{tG}

Figure 7.2.: Dependence of the limits on integrated luminosity if an ideal fit function is used to model the cross-section as a function of the Wilson coefficients.

and detector simulation (AFII) are being generated so that comparisons can be made directly at the detector level. The production of these samples is computationally expensive. Also, it has to be done by the ATLAS central production team and cannot be done locally. Hence these samples are not yet ready, and this part has not been included in this analysis.

7.0.5. Other studies

This analysis was designed to study the top-photon vertex. The $t\bar{t}\gamma$ process was chosen for this purpose as it includes events where a photon is radiated directly from the top quark and hence has higher sensitivity to this vertex. The developed analysis technique can be used to study other top-couplings. For example, the kinematics of the Z boson can be analysed to understand the weak interaction better. For this, a study should be done on the $t\bar{t}Z$ process, as this process would be more sensitive to the top-Z boson vertex. A similar study can also be done on $t\bar{t}H$ process to understand the Higgs coupling to the top quark.

For each of these two cases, the relevant EFT operators can be identified, and limits can be extracted on the corresponding Wilson coefficients. But these studies will be more difficult

and will have more uncertainties than the studies on $t\bar{t}\gamma$. This is because photons are easier to identify and reconstruct than Z or Higgs boson, which have to be reconstructed from their decay products.

A. EFT Parametrisation functions

A.0.1. The fit function for all the 16 bins in the photon p_{T} distribution

Bin 1 = 5.36594 +C_{tG}*1.08909 +C_{tG}*C_{tG}*0.142493 +C_{tG}*C_{tW}*0.274728 +C_{tW}*1.21809 +C_{tW}*C_{tW}*0.191228 +C_{tW}*C_{tZ}* -0.0421518 +C_{tZ}* -0.00409978 +C_{tZ}*C_{tG}*0.00089041 +C_{tZ}*C_{tZ}*0.0109672

Bin 2 = 4.2983 +C_{tG}*0.889755 +C_{tG}*C_{tG}* -0.122166 +C_{tG}*C_{tW}*0.26998 +C_{tW}*0.971638 +C_{tW}*C_{tW}*0.12092 +C_{tW}*C_{tZ}* -0.0682231 +C_{tZ}* -0.0263854 +C_{tZ}*C_{tG}*0.0096366 +C_{tZ}*C_{tZ}*0.0227467

Bin 3 = 3.5492 +C_{tG}*0.759639 +C_{tG}*C_{tG}*0.0108487 +C_{tG}*C_{tW}*0.207279 +C_{tW}*0.80534 +C_{tW}*C_{tW}*0.131474 +C_{tW}*C_{tZ}* -0.050807 +C_{tZ}* -0.0243516 +C_{tZ}*C_{tG}*0.00557761 +C_{tZ}*C_{tZ}*0.0343008

Bin 4 = 2.9244 +C_{tG}*0.583985 +C_{tG}*C_{tG}*0.218036 +C_{tG}*C_{tW}*0.144482 +C_{tW}*0.657298 +C_{tW}*C_{tW}*0.0928738 +C_{tW}*C_{tZ}* -0.0232478 +C_{tZ}* -0.0192989 +C_{tZ}*C_{tG}*0.00980613 +C_{tZ}*C_{tZ}*0.0314106

Bin 5 = 2.43719 +C_{tG}*0.544439 +C_{tG}*C_{tG}*0.401363 +C_{tG}*C_{tW}*0.153331 +C_{tW}*0.578971 +C_{tW}*C_{tW}*0.148178 +C_{tW}*C_{tZ}* -0.0437224 +C_{tZ}* -0.0310228 +C_{tZ}*C_{tG}* -0.0163047 +C_{tZ}*C_{tZ}*0.0651749

Bin 6 = 3.32691 +C_{tG}*0.659452 +C_{tG}*C_{tG}* -0.052178 +C_{tG}*C_{tW}*0.192372 +C_{tW}*0.76244 +C_{tW}*C_{tW}*0.156463 +C_{tW}*C_{tZ}* -0.0755405 +C_{tZ}* -0.0321919 +C_{tZ}*C_{tG}*0.0105589 +C_{tZ}*C_{tZ}*0.047009

Bin 7 = 2.51702 +C_{tG}*0.487623 +C_{tG}*C_{tG}*0.17766 +C_{tG}*C_{tW}*0.143703 +C_{tW}*0.58919 +C_{tW}*C_{tW}*0.135541 +C_{tW}*C_{tZ}* -0.0796543 +C_{tZ}* -0.0433925 +C_{tZ}*C_{tG}* -0.044831 +C_{tZ}*C_{tZ}*0.0401568

Bin 8 = 1.98657 +C_{tG}*0.40665 +C_{tG}*C_{tG}*0.168036 +C_{tG}*C_{tW}*0.122393 +C_{tW}*0.478315 +C_{tW}*C_{tW}*0.129437 +C_{tW}*C_{tZ}* -0.0696283 +C_{tZ}* -0.0355266 +C_{tZ}*C_{tG}* -0.043006 +C_{tZ}*C_{tZ}*0.0460713

Bin 9 = 1.63934 +C_{tG}*0.303827 +C_{tG}*C_{tG}*0.082584 +C_{tG}*C_{tW}*0.0650823 +C_{tW}*0.37412 +C_{tW}*C_{tW}*0.0792857 +C_{tW}*C_{tZ}* -0.0773784 +C_{tZ}* -0.030508 +C_{tZ}*C_{tG}* -0.00481607 +C_{tZ}*C_{tZ}*0.0335518

Bin 10 = 2.36194 +C_{tG}*0.486802 +C_{tG}*C_{tG}*0.0186563 +C_{tG}*C_{tW}*0.183267 +C_{tW}*0.612281 +C_{tW}*C_{tW}*0.182793 +C_{tW}*C_{tZ}* -0.16995 +C_{tZ}* -0.0877826 +C_{tZ}*C_{tG}* -0.0125999 +C_{tZ}*C_{tZ}*0.0581085

Bin 11 = 1.64695 +C_{tG}*0.334549 +C_{tG}*C_{tG}*0.151356 +C_{tG}*C_{tW}*0.108796 +C_{tW}*0.439191 +C_{tW}*C_{tW}*0.162041 +C_{tW}*C_{tZ}* -0.140969 +C_{tZ}* -0.0665387 +C_{tZ}*C_{tG}*0.0145437 +C_{tZ}*C_{tZ}*0.0808295
Bin 12 = 1.18186 +C_{tG}*0.269735 +C_{tG}*C_{tG}* -0.0819327 +C_{tG}*C_{tW}*0.0898474 +C_{tW}*0.327125 +C_{tW}*C_{tW}*0.110652 +C_{tW}*C_{tZ}* -0.139526 +C_{tZ}* -0.0636678 +C_{tZ}*C_{tG}*6.1372e -05 +C_{tZ}*C_{tZ}*0.0550297
Bin 13 = 1.26117 +C_{tG}*0.262294 +C_{tG}*C_{tG}*0.238067 +C_{tG}*C_{tW}*0.088879 +C_{tW}*0.367147 +C_{tW}*C_{tW}*0.18245 +C_{tW}*C_{tZ}* -0.211664 +C_{tZ}* -0.0932278 +C_{tZ}*C_{tG}* -0.0121042 +C_{tZ}*C_{tZ}*0.0997453
Bin 14 = 1.5046 +C_{tG}*0.342968 +C_{tG}*C_{tG}*0.0959147 +C_{tG}*C_{tW}*0.173693 +C_{tW}*0.472098 +C_{tW}*C_{tW}*0.278805 +C_{tW}*C_{tZ}* -0.368237 +C_{tZ}* -0.138652 +C_{tZ}*C_{tG}* -0.00220359 +C_{tZ}*C_{tZ}*0.170238
Bin 15 = 1.20619 +C_{tG}*0.307513 +C_{tG}*C_{tG}*0.0448984 +C_{tG}*C_{tW}*0.115115 +C_{tW}*0.453986 +C_{tW}*C_{tW}*0.348541 +C_{tW}*C_{tZ}* -0.517461 +C_{tZ}* -0.16999 +C_{tZ}*C_{tG}*0.0262324 +C_{tZ}*C_{tZ}*0.227916
Bin 16 = 0.908855 +C_{tG}*0.285347 +C_{tG}*C_{tG}*0.173556 +C_{tG}*C_{tW}*0.0976672 +C_{tW}*0.467477 +C_{tW}*C_{tW}*0.591693 +C_{tW}*C_{tZ}* -0.905207 +C_{tZ}* -0.221091 +C_{tZ}*C_{tG}* -0.00946917 +C_{tZ}*C_{tZ}*0.414074

A.0.2. The fit function for all the 16 bins in the photon $|\eta|$ distribution

Bin 1 = 2.50706 + C_{tG}*0.585603 + C_{tG}*C_{tG}*0.36304 + C_{tG}*C_{tW}*0.202514 + C_{tW}*0.646746 + C_{tW}*C_{tW}*0.254342 + C_{tW}*C_{tZ}*-0.267436 + C_{tZ}*-0.0774951 + C_{tZ}*C_{tG}*0.000144649 + C_{tZ}*C_{tZ}*0.147688
Bin 2 = 2.52113 + C_{tG}*0.5669 + C_{tG}*C_{tG}*0.116286 + C_{tG}*C_{tW}*0.189327 + C_{tW}*0.66484 + C_{tW}*C_{tW}*0.250302 + C_{tW}*C_{tZ}*-0.27301 + C_{tZ}*-0.0740248 + C_{tZ}*C_{tG}*0.0490424 + C_{tZ}*C_{tZ}*0.117123
Bin 3 = 2.49361 + C_{tG}*0.570679 + C_{tG}*C_{tG}*0.293362 + C_{tG}*C_{tW}*0.204935 + C_{tW}*0.657439 + C_{tW}*C_{tW}*0.260698 + C_{tW}*C_{tZ}*-0.267742 + C_{tZ}*-0.0827759 + C_{tZ}*C_{tG}*-0.0156223 + C_{tZ}*C_{tZ}*0.13594
Bin 4 = 2.39994 + C_{tG}*0.535201 + C_{tG}*C_{tG}*0.364715 + C_{tG}*C_{tW}*0.211628 + C_{tW}*0.646904 + C_{tW}*C_{tW}*0.256106 + C_{tW}*C_{tZ}*-0.242954 + C_{tZ}*-0.0767885 + C_{tZ}*C_{tG}*0.0116526 + C_{tZ}*C_{tZ}*0.14204
Bin 5 = 2.3742 + C_{tG}*0.529139 + C_{tG}*C_{tG}*0.0277372 + C_{tG}*C_{tW}*0.177948 + C_{tW}*0.626585 + C_{tW}*C_{tW}*0.236416 + C_{tW}*C_{tZ}*-0.234515 + C_{tZ}*-0.0718184 + C_{tZ}*C_{tG}*0.00109925 + C_{tZ}*C_{tZ}*0.124685
Bin 6 = 2.33103 + C_{tG}*0.571118 + C_{tG}*C_{tG}*0.12895 + C_{tG}*C_{tW}*0.160556 + C_{tW}*0.600412 + C_{tW}*C_{tW}*0.219295 + C_{tW}*C_{tZ}*-0.221846 + C_{tZ}*-0.0717909 + C_{tZ}*C_{tG}*-0.01065

+ C_{tZ}*C_{tZ}*0.129068

Bin 7 = 2.24205 + C_{tG}*0.55058 + C_{tG}*C_{tG}*0.256745 + C_{tG}*C_{tW}*0.156425 + C_{tW}*0.58076
+ C_{tW}*C_{tW}*0.221441 + C_{tW}*C_{tZ}*-0.23983 + C_{tZ}*-0.0796458 + C_{tZ}*C_{tG}*-0.00939805
+ C_{tZ}*C_{tZ}*0.125819

Bin 8 = 2.17694 + C_{tG}*0.456319 + C_{tG}*C_{tG}*0.0462949 + C_{tG}*C_{tW}*0.101445 + C_{tW}*0.567029
+ C_{tW}*C_{tW}*0.216771 + C_{tW}*C_{tZ}*-0.217736 + C_{tZ}*-0.0628288 + C_{tZ}*C_{tG}*-0.0178434
+ C_{tZ}*C_{tZ}*0.0997241

Bin 9 = 2.0632 + C_{tG}*0.414396 + C_{tG}*C_{tG}*0.0357581 + C_{tG}*C_{tW}*0.0874405 + C_{tW}*0.539036
+ C_{tW}*C_{tW}*0.186317 + C_{tW}*C_{tZ}*-0.211076 + C_{tZ}*-0.0654896 + C_{tZ}*C_{tG}*0.0247562
+ C_{tZ}*C_{tZ}*0.0942789

Bin 10 = 1.92476 + C_{tG}*0.456273 + C_{tG}*C_{tG}*-0.0250657 + C_{tG}*C_{tW}*0.136794 + C_{tW}*0.517113
+ C_{tW}*C_{tW}*0.174239 + C_{tW}*C_{tZ}*-0.188757 + C_{tZ}*-0.0538122 + C_{tZ}*C_{tG}*0.0330439
+ C_{tZ}*C_{tZ}*0.0794356

Bin 11 = 1.82229 + C_{tG}*0.425416 + C_{tG}*C_{tG}*0.00194258 + C_{tG}*C_{tW}*0.104685 + C_{tW}*0.489707
+ C_{tW}*C_{tW}*0.163166 + C_{tW}*C_{tZ}*-0.17961 + C_{tZ}*-0.06597 + C_{tZ}*C_{tG}*0.0270307
+ C_{tZ}*C_{tZ}*0.0921233

Bin 12 = 1.71862 + C_{tG}*0.351344 + C_{tG}*C_{tG}*0.130238 + C_{tG}*C_{tW}*0.0876441 + C_{tW}*0.46468
+ C_{tW}*C_{tW}*0.176496 + C_{tW}*C_{tZ}*-0.170569 + C_{tZ}*-0.0683698 + C_{tZ}*C_{tG}*0.0106038
+ C_{tZ}*C_{tZ}*0.0851101

Bin 13 = 3.07902 + C_{tG}*0.716672 + C_{tG}*C_{tG}*0.256297 + C_{tG}*C_{tW}*0.218345 + C_{tW}*0.814448
+ C_{tW}*C_{tW}*0.287313 + C_{tW}*C_{tZ}*-0.293057 + C_{tZ}*-0.106248 + C_{tZ}*C_{tG}*-0.0339969
+ C_{tZ}*C_{tZ}*0.144934

Bin 14 = 3.77958 + C_{tG}*0.837202 + C_{tG}*C_{tG}*-0.14064 + C_{tG}*C_{tW}*0.299151 + C_{tW}*0.961544
+ C_{tW}*C_{tW}*0.310645 + C_{tW}*C_{tZ}*-0.341187 + C_{tZ}*-0.149671 + C_{tZ}*C_{tG}*-0.03216
+ C_{tZ}*C_{tZ}*0.134852

Bin 15 = 2.71704 + C_{tG}*0.53421 + C_{tG}*C_{tG}*0.196963 + C_{tG}*C_{tW}*0.149552 + C_{tW}*0.69023
+ C_{tW}*C_{tW}*0.216166 + C_{tW}*C_{tZ}*-0.219743 + C_{tZ}*-0.101323 + C_{tZ}*C_{tG}*0.0165631
+ C_{tZ}*C_{tZ}*0.104745

Bin 16 = 2.25155 + C_{tG}*0.39966 + C_{tG}*C_{tG}*0.000302506 + C_{tG}*C_{tW}*0.111953 + C_{tW}*0.520158
+ C_{tW}*C_{tW}*0.164289 + C_{tW}*C_{tZ}*-0.170759 + C_{tZ}*-0.0812136 + C_{tZ}*C_{tG}*-0.0159636
+ C_{tZ}*C_{tZ}*0.0505986

A.0.3. The fit function for all the 16 bins in the photon $\Delta R_{min}(\gamma, \ell)$ distribution

Bin1 = 4.11556 + ctg*0.888731 + ctg*ctg*0.354993 + ctg*ctw*0.238034 + ctw*0.923109
+ ctw*ctw*0.195995 + C_{tW}*C_{tZ}*-0.0658494 + C_{tZ}*-0.0308705 + C_{tZ}*C_{tG}*-0.027333
+ C_{tZ}*C_{tZ}*0.0624098

Bin2 = 3.42886 + C_{tG}*0.670982 + C_{tG}*C_{tG}*0.369633 + C_{tG}*C_{tW}*0.229214 + C_{tW}*0.76974
+ C_{tW}*C_{tW}*0.166818 + C_{tW}*C_{tZ}*-0.0715886 + C_{tZ}*-0.0401692 + C_{tZ}*C_{tG}*-0.0361812
+ C_{tZ}*C_{tZ}*0.052499
Bin3 = 2.87503 + C_{tG}*0.631291 + C_{tG}*C_{tG}*0.232652 + C_{tG}*C_{tW}*0.195361 + C_{tW}*0.66018
+ C_{tW}*C_{tW}*0.153966 + C_{tW}*C_{tZ}*-0.0760181 + C_{tZ}*-0.0523361 + C_{tZ}*C_{tG}*-0.0305438
+ C_{tZ}*C_{tZ}*0.0716986
Bin4 = 2.46398 + C_{tG}*0.565498 + C_{tG}*C_{tG}*-0.088392 + C_{tG}*C_{tW}*0.201851 + C_{tW}*0.598547
+ C_{tW}*C_{tW}*0.109284 + C_{tW}*C_{tZ}*-0.0928642 + C_{tZ}*-0.0441438 + C_{tZ}*C_{tG}*0.0137899
+ C_{tZ}*C_{tZ}*0.0423053
Bin5 = 2.21553 + C_{tG}*0.463727 + C_{tG}*C_{tG}*0.0618886 + C_{tG}*C_{tW}*0.14961 + C_{tW}*0.551628
+ C_{tW}*C_{tW}*0.129217 + C_{tW}*C_{tZ}*-0.101652 + C_{tZ}*-0.031776 + C_{tZ}*C_{tG}*-0.00329803
+ C_{tZ}*C_{tZ}*0.0541695
Bin6 = 2.01165 + C_{tG}*0.400745 + C_{tG}*C_{tG}*-0.0118613 + C_{tG}*C_{tW}*0.103051 + C_{tW}*0.506884
+ C_{tW}*C_{tW}*0.132102 + C_{tW}*C_{tZ}*-0.120047 + C_{tZ}*-0.0600086 + C_{tZ}*C_{tG}*0.0358481
+ C_{tZ}*C_{tZ}*0.0623383
Bin7 = 3.61494 + C_{tG}*0.737627 + C_{tG}*C_{tG}*0.216928 + C_{tG}*C_{tW}*0.170473 + C_{tW}*0.938463
+ C_{tW}*C_{tW}*0.319935 + C_{tW}*C_{tZ}*-0.259738 + C_{tZ}*-0.0967356 + C_{tZ}*C_{tG}*0.00925232
+ C_{tZ}*C_{tZ}*0.13195
Bin8 = 3.15843 + C_{tG}*0.743783 + C_{tG}*C_{tG}*0.238174 + C_{tG}*C_{tW}*0.217001 + C_{tW}*0.873222
+ C_{tW}*C_{tW}*0.312774 + C_{tW}*C_{tZ}*-0.306329 + C_{tZ}*-0.102387 + C_{tZ}*C_{tG}*0.0204031
+ C_{tZ}*C_{tZ}*0.137411
Bin9 = 2.75986 + C_{tG}*0.607866 + C_{tG}*C_{tG}*-0.0214719 + C_{tG}*C_{tW}*0.189857 + C_{tW}*0.796664
+ C_{tW}*C_{tW}*0.277078 + C_{tW}*C_{tZ}*-0.338857 + C_{tZ}*-0.107388 + C_{tZ}*C_{tG}*8.30376e-05
+ C_{tZ}*C_{tZ}*0.143186
Bin10 = 2.49208 + C_{tG}*0.577534 + C_{tG}*C_{tG}*0.0967376 + C_{tG}*C_{tW}*0.181732 + C_{tW}*0.70231
+ C_{tW}*C_{tW}*0.293781 + C_{tW}*C_{tZ}*-0.353869 + C_{tZ}*-0.118893 + C_{tZ}*C_{tG}*0.000208455
+ C_{tZ}*C_{tZ}*0.164667
Bin11 = 2.14617 + C_{tG}*0.556689 + C_{tG}*C_{tG}*0.351131 + C_{tG}*C_{tW}*0.190239 + C_{tW}*0.653654
+ C_{tW}*C_{tW}*0.316803 + C_{tW}*C_{tZ}*-0.366512 + C_{tZ}*-0.111082 + C_{tZ}*C_{tG}*-0.017061
+ C_{tZ}*C_{tZ}*0.169816
Bin12 = 2.62039 + C_{tG}*0.63185 + C_{tG}*C_{tG}*0.102395 + C_{tG}*C_{tW}*0.189569 + C_{tW}*0.777124
+ C_{tW}*C_{tW}*0.381451 + C_{tW}*C_{tZ}*-0.538371 + C_{tZ}*-0.164255 + C_{tZ}*C_{tG}*0.0126482
+ C_{tZ}*C_{tZ}*0.245801
Bin13 = 2.44783 + C_{tG}*0.582592 + C_{tG}*C_{tG}*-0.0583117 + C_{tG}*C_{tW}*0.187932 + C_{tW}*0.727729
+ C_{tW}*C_{tW}*0.444635 + C_{tW}*C_{tZ}*-0.578623 + C_{tZ}*-0.187128 + C_{tZ}*C_{tG}*0.0217272
+ C_{tZ}*C_{tZ}*0.264106
Bin14 = 1.91249 + C_{tG}*0.382723 + C_{tG}*C_{tG}*0.142933 + C_{tG}*C_{tW}*0.144883 + C_{tW}*0.467069
+ C_{tW}*C_{tW}*0.339011 + C_{tW}*C_{tZ}*-0.468213 + C_{tZ}*-0.123035 + C_{tZ}*C_{tG}*0.0128122
+ C_{tZ}*C_{tZ}*0.207122

A.0.4. The fit function for all the 16 bins in the photon $\Delta\eta(\ell,\ell)$ distribution

Bin1 = 3.64181 + C_{tG}*0.921586 + C_{tG}*C_{tG}*0.22311 + C_{tG}*C_{tW}*0.279163 + C_{tW}*1.06812
+ C_{tW}*C_{tW}*0.366459 + C_{tW}*C_{tZ}*-0.353357 + C_{tZ}*-0.153595 + C_{tZ}*C_{tG}*-0.00907912
+ C_{tZ}*C_{tZ}*0.183617

Bin2 = 3.70663 + C_{tG}*0.896606 + C_{tG}*C_{tG}*0.129908 + C_{tG}*C_{tW}*0.27591 + C_{tW}*1.07692
+ C_{tW}*C_{tW}*0.390407 + C_{tW}*C_{tZ}*-0.379972 + C_{tZ}*-0.15677 + C_{tZ}*C_{tG}*-0.0338664
+ C_{tZ}*C_{tZ}*0.188075

Bin3 = 3.75636 + C_{tG}*0.928634 + C_{tG}*C_{tG}*0.447808 + C_{tG}*C_{tW}*0.294927 + C_{tW}*1.06737
+ C_{tW}*C_{tW}*0.385111 + C_{tW}*C_{tZ}*-0.384597 + C_{tZ}*-0.178677 + C_{tZ}*C_{tG}*0.0208997
+ C_{tZ}*C_{tZ}*0.210373

Bin4 = 3.64494 + C_{tG}*0.859522 + C_{tG}*C_{tG}*0.177081 + C_{tG}*C_{tW}*0.276957 + C_{tW}*1.01846
+ C_{tW}*C_{tW}*0.373067 + C_{tW}*C_{tZ}*-0.35745 + C_{tZ}*-0.146475 + C_{tZ}*C_{tG}*0.0890481
+ C_{tZ}*C_{tZ}*0.166207

Bin5 = 3.49465 + C_{tG}*0.825653 + C_{tG}*C_{tG}*-0.0339647 + C_{tG}*C_{tW}*0.257487 + C_{tW}*0.947741
+ C_{tW}*C_{tW}*0.313939 + C_{tW}*C_{tZ}*-0.347983 + C_{tZ}*-0.136173 + C_{tZ}*C_{tG}*-0.010092
+ C_{tZ}*C_{tZ}*0.170554

Bin6 = 3.27473 + C_{tG}*0.746877 + C_{tG}*C_{tG}*0.425755 + C_{tG}*C_{tW}*0.231758 + C_{tW}*0.859625
+ C_{tW}*C_{tW}*0.32692 + C_{tW}*C_{tZ}*-0.324383 + C_{tZ}*-0.123851 + C_{tZ}*C_{tG}*0.0177149
+ C_{tZ}*C_{tZ}*0.155724

Bin7 = 3.00419 + C_{tG}*0.68387 + C_{tG}*C_{tG}*0.107811 + C_{tG}*C_{tW}*0.220003 + C_{tW}*0.78074
+ C_{tW}*C_{tW}*0.281422 + C_{tW}*C_{tZ}*-0.285598 + C_{tZ}*-0.101624 + C_{tZ}*C_{tG}*-0.0362323
+ C_{tZ}*C_{tZ}*0.155347

Bin8 = 2.66132 + C_{tG}*0.59964 + C_{tG}*C_{tG}*0.114517 + C_{tG}*C_{tW}*0.17866 + C_{tW}*0.670638
+ C_{tW}*C_{tW}*0.252051 + C_{tW}*C_{tZ}*-0.24678 + C_{tZ}*-0.0578241 + C_{tZ}*C_{tG}*-0.0206433
+ C_{tZ}*C_{tZ}*0.0896821

Bin9 = 2.35726 + C_{tG}*0.486922 + C_{tG}*C_{tG}*0.0881269 + C_{tG}*C_{tW}*0.148866 + C_{tW}*0.576223
+ C_{tW}*C_{tW}*0.202331 + C_{tW}*C_{tZ}*-0.228376 + C_{tZ}*-0.0611721 + C_{tZ}*C_{tG}*-0.0110881
+ C_{tZ}*C_{tZ}*0.0937644

Bin10 = 2.01557 + C_{tG}*0.385356 + C_{tG}*C_{tG}*0.153571 + C_{tG}*C_{tW}*0.113621 + C_{tW}*0.483315
+ C_{tW}*C_{tW}*0.17917 + C_{tW}*C_{tZ}*-0.189668 + C_{tZ}*-0.0510229 + C_{tZ}*C_{tG}*-0.0114354
+ C_{tZ}*C_{tZ}*0.101839

Bin11 = 1.76832 + C_{tG}*0.319825 + C_{tG}*C_{tG}*0.0638771 + C_{tG}*C_{tW}*0.0948345 + C_{tW}*0.394256
+ C_{tW}*C_{tW}*0.127923 + C_{tW}*C_{tZ}*-0.162625 + C_{tZ}*-0.0421722 + C_{tZ}*C_{tG}*0.0200735
+ C_{tZ}*C_{tZ}*0.0762895

Bin12 = 5.07623 + C_{tG}*0.849478 + C_{tG}*C_{tG}*0.156361 + C_{tG}*C_{tW}*0.227148 + C_{tW}*1.04529

+ C_{tW}*C_{tW}*0.395301 + C_{tW}*C_{tZ}*-0.477468 + C_{tZ}*-0.0794283 + C_{tZ}*C_{tG}*0.0262249
+ C_{tZ}*C_{tZ}*0.217506

A.0.5. The fit function for all the 16 bins in the photon $\Delta\phi(\ell,\ell)$ distribution

Bin1 = 3.17207 + C_{tG}*0.609016 + C_{tG}*C_{tG}*0.142259 + C_{tG}*C_{tW}*0.181856 + C_{tW}*0.606893
+ C_{tW}*C_{tW}*0.315403 + C_{tW}*C_{tZ}*-0.364887 + C_{tZ}*-0.109991 + C_{tZ}*C_{tG}*0.00582879
+ C_{tZ}*C_{tZ}*0.186275
Bin2 = 3.26992 + C_{tG}*0.60904 + C_{tG}*C_{tG}*-0.102236 + C_{tG}*C_{tW}*0.164524 + C_{tW}*0.620696
+ C_{tW}*C_{tW}*0.254012 + C_{tW}*C_{tZ}*-0.346666 + C_{tZ}*-0.103281 + C_{tZ}*C_{tG}*0.000141402
+ C_{tZ}*C_{tZ}*0.153215
Bin3 = 2.71748 + C_{tG}*0.553266 + C_{tG}*C_{tG}*0.0621098 + C_{tG}*C_{tW}*0.137343 + C_{tW}*0.589301
+ C_{tW}*C_{tW}*0.230156 + C_{tW}*C_{tZ}*-0.289602 + C_{tZ}*-0.0970252 + C_{tZ}*C_{tG}*0.0275371
+ C_{tZ}*C_{tZ}*0.131661
Bin4 = 3.10072 + C_{tG}*0.664628 + C_{tG}*C_{tG}*0.158952 + C_{tG}*C_{tW}*0.224136 + C_{tW}*0.690511
+ C_{tW}*C_{tW}*0.284414 + C_{tW}*C_{tZ}*-0.315386 + C_{tZ}*-0.118873 + C_{tZ}*C_{tG}*0.0036136
+ C_{tZ}*C_{tZ}*0.17201
Bin5 = 2.33119 + C_{tG}*0.516702 + C_{tG}*C_{tG}*0.0911127 + C_{tG}*C_{tW}*0.163007 + C_{tW}*0.553682
+ C_{tW}*C_{tW}*0.199142 + C_{tW}*C_{tZ}*-0.228208 + C_{tZ}*-0.0500664 + C_{tZ}*C_{tG}*0.0549965
+ C_{tZ}*C_{tZ}*0.0994008
Bin6 = 2.57512 + C_{tG}*0.593808 + C_{tG}*C_{tG}*0.29302 + C_{tG}*C_{tW}*0.168502 + C_{tW}*0.626443
+ C_{tW}*C_{tW}*0.228054 + C_{tW}*C_{tZ}*-0.248353 + C_{tZ}*-0.0924618 + C_{tZ}*C_{tG}*0.0121147
+ C_{tZ}*C_{tZ}*0.130337
Bin7 = 2.89449 + C_{tG}*0.629912 + C_{tG}*C_{tG}*0.400949 + C_{tG}*C_{tW}*0.161363 + C_{tW}*0.759623
+ C_{tW}*C_{tW}*0.283164 + C_{tW}*C_{tZ}*-0.259012 + C_{tZ}*-0.0762069 + C_{tZ}*C_{tG}*0.0375043
+ C_{tZ}*C_{tZ}*0.135954
Bin8 = 3.09014 + C_{tG}*0.743036 + C_{tG}*C_{tG}*0.279983 + C_{tG}*C_{tW}*0.232405 + C_{tW}*0.862609
+ C_{tW}*C_{tW}*0.29231 + C_{tW}*C_{tZ}*-0.277791 + C_{tZ}*-0.104817 + C_{tZ}*C_{tG}*0.0251414
+ C_{tZ}*C_{tZ}*0.161188
Bin9 = 3.33476 + C_{tG}*0.808488 + C_{tG}*C_{tG}*0.26104 + C_{tG}*C_{tW}*0.312645 + C_{tW}*0.959269
+ C_{tW}*C_{tW}*0.31445 + C_{tW}*C_{tZ}*-0.310431 + C_{tZ}*-0.10793 + C_{tZ}*C_{tG}*-0.0483526
+ C_{tZ}*C_{tZ}*0.136281
Bin10 = 1.75585 + C_{tG}*0.436321 + C_{tG}*C_{tG}*0.0537493 + C_{tG}*C_{tW}*0.11033 + C_{tW}*0.516463
+ C_{tW}*C_{tW}*0.15137 + C_{tW}*C_{tZ}*-0.165633 + C_{tZ}*-0.0590422 + C_{tZ}*C_{tG}*0.0102546
+ C_{tZ}*C_{tZ}*0.0786478
Bin11 = 1.7974 + C_{tG}*0.391481 + C_{tG}*C_{tG}*0.0189036 + C_{tG}*C_{tW}*0.131682 + C_{tW}*0.5353
+ C_{tW}*C_{tW}*0.163762 + C_{tW}*C_{tZ}*-0.166061 + C_{tZ}*-0.0602787 + C_{tZ}*C_{tG}*-0.00114547

$+ C_{tZ}*C_{tZ}*0.0768295$

$\text{Bin12} = 1.87882 + C_{tG}*0.443758 + C_{tG}*C_{tG}*0.205103 + C_{tG}*C_{tW}*0.156036 + C_{tW}*0.580755$
$+ C_{tW}*C_{tW}*0.204667 + C_{tW}*C_{tZ}*-0.160403 + C_{tZ}*-0.0649014 + C_{tZ}*C_{tG}*-0.0235938$
$+ C_{tZ}*C_{tZ}*0.0817657$

$\text{Bin13} = 1.85588 + C_{tG}*0.422986 + C_{tG}*C_{tG}*-0.00802973 + C_{tG}*C_{tW}*0.102117 + C_{tW}*0.593719$
$+ C_{tW}*C_{tW}*0.169326 + C_{tW}*C_{tZ}*-0.170191 + C_{tZ}*-0.0562829 + C_{tZ}*C_{tG}*-0.0425269$
$+ C_{tZ}*C_{tZ}*0.0585579$

$\text{Bin14} = 1.92329 + C_{tG}*0.433895 + C_{tG}*C_{tG}*0.20544 + C_{tG}*C_{tW}*0.125176 + C_{tW}*0.616821$
$+ C_{tW}*C_{tW}*0.205877 + C_{tW}*C_{tZ}*-0.190518 + C_{tZ}*-0.0800421 + C_{tZ}*C_{tG}*-0.0265424$
$+ C_{tZ}*C_{tZ}*0.0884716$

$\text{Bin15} = 2.69046 + C_{tG}*0.634564 + C_{tG}*C_{tG}*-0.000631766 + C_{tG}*C_{tW}*0.22457 + C_{tW}*0.86099$
$+ C_{tW}*C_{tW}*0.291893 + C_{tW}*C_{tZ}*-0.244023 + C_{tZ}*-0.104322 + C_{tZ}*C_{tG}*0.00335257$
$+ C_{tZ}*C_{tZ}*0.118328$

B. Correlation between observables

B.0.1. Correlation factor between Photon p_{T} and $\Delta R_{min}(\gamma, \ell)$

Sample			Correlation	Sample			Correlation	Sample			Correlation
ctW	ctZ	ctG	factor	ctW	ctZ	ctG	factor	ctW	ctZ	ctG	factor
0	0	0	0.185	1	1.4	0.4	0.197	-1.2	-1	0	0.208
0	0	0.4	0.185	1	-1	0.4	0.313	0	1.4	-0.4	0.264
0	0	-0.4	0.192	-1.2	1.4	0.4	0.339	1	1.4	-0.4	0.191
0	1.4	0	0.268	-1.2	-1	0.4	0.197	-1.2	1.4	-0.4	0.334
0	-1	0	0.240	1	0	0.4	0.250	1	0	-0.4	0.246
1	0	0	0.244	-1.2	0	0.4	0.262	-1.2	0	-0.4	0.267
-1.2	0	0	0.259	1	1.4	0	0.200	1	-1	-0.4	0.301
0	1.4	0.4	0.261	-1.2	1.4	0	0.333	0	-1	-0.4	0.234
0	-1	0.4	0.236	1	-1	0	0.304	-1.2	-1	-0.4	0.188

B.0.2. Correlation factor between Photon p_{T} and $\Delta\eta(\ell, \ell)$

Sample			Correlation	Sample			Correlation	Sample			Correlation
ctW	ctZ	ctG	factor	ctW	ctZ	ctG	factor	ctW	ctZ	ctG	factor
0	0	0	0.025	1	1.4	0.4	0.044	-1.2	-1	0	0.042
0	0	0.4	0.037	1	-1	0.4	0.017	0	1.4	-0.4	0.050
0	0	-0.4	0.031	-1.2	1.4	0.4	0.054	1	1.4	-0.4	0.044
0	1.4	0	0.058	-1.2	-1	0.4	0.043	-1.2	1.4	-0.4	0.049
0	-1	0	0.020	1	0	0.4	0.015	1	0	-0.4	0.026
1	0	0	0.027	-1.2	0	0.4	0.064	-1.2	0	-0.4	0.057
-1.2	0	0	0.065	1	1.4	0	0.032	1	-1	-0.4	0.034
0	1.4	0.4	0.062	-1.2	1.4	0	0.062	0	-1	-0.4	0.017
0	-1	0.4	0.014	1	-1	0	0.025	-1.2	-1	-0.4	0.042

B.0.3. Correlation factor between Photon p_{T} and $\Delta\eta(\ell,\ell)$

Sample			Correlation	Sample			Correlation	Sample			Correlation
ctW	ctZ	ctG	factor	ctW	ctZ	ctG	factor	ctW	ctZ	ctG	factor
0	0	0	-0.0027	1	1.4	0.4	-0.0140	-1.2	-1	0	-0.0214
0	0	0.4	-0.0048	1	-1	0.4	-0.0718	0	1.4	-0.4	-0.0519
0	0	-0.4	-0.0159	-1.2	1.4	0.4	-0.0958	1	1.4	-0.4	-0.0103
0	1.4	0	-0.0507	-1.2	-1	0.4	-0.0085	-1.2	1.4	-0.4	-0.0972
0	-1	0	-0.0259	1	0	0.4	-0.0347	1	0	-0.4	-0.0470
1	0	0	-0.0355	-1.2	0	0.4	-0.0504	-1.2	0	-0.4	-0.0515
-1.2	0	0	-0.0464	1	1.4	0	-0.0165	1	-1	-0.4	-0.0762
0	1.4	0.4	-0.0441	-1.2	1.4	0	-0.0931	0	-1	-0.4	-0.0377
0	-1	0.4	-0.0242	1	-1	0	-0.0811	-1.2	-1	-0.4	-0.0030

B.0.4. Correlation factor between Photon $|\eta|$ and $\Delta R_{min}(\gamma,\ell)$

Sample			Correlation	Sample			Correlation	Sample			Correlation
ctW	ctZ	ctG	factor	ctW	ctZ	ctG	factor	ctW	ctZ	ctG	factor
0	0	0	0.0334	1	1.4	0.4	0.0526	-1.2	-1	0	0.0468
0	0	0.4	0.0542	1	-1	0.4	0.0457	0	1.4	-0.4	0.0306
0	0	-0.4	0.0569	-1.2	1.4	0.4	0.0231	1	1.4	-0.4	0.0511
0	1.4	0	0.0424	-1.2	-1	0.4	0.0466	-1.2	1.4	-0.4	0.0251
0	-1	0	0.0529	1	0	0.4	0.0390	1	0	-0.4	0.0501
1	0	0	0.0473	-1.2	0	0.4	0.0439	-1.2	0	-0.4	0.0460
-1.2	0	0	0.0247	1	1.4	0	0.0625	1	-1	-0.4	0.0528
0	1.4	0.4	0.0482	-1.2	1.4	0	0.0162	0	-1	-0.4	0.0523
0	-1	0.4	0.0503	1	-1	0	0.0473	-1.2	-1	-0.4	0.0510

B.0.5. Correlation factor between Photon $|\eta|$ and $\Delta\eta(\ell,\ell)$

Sample			Correlation	Sample			Correlation	Sample			Correlation
ctW	ctZ	ctG	factor	ctW	ctZ	ctG	factor	ctW	ctZ	ctG	factor
0	0	0	0.0046	1	1.4	0.4	0.0176	-1.2	-1	0	0.0207
0	0	0.4	0.0132	1	-1	0.4	0.0076	0	1.4	-0.4	0.0035
0	0	-0.4	0.0013	-1.2	1.4	0.4	0.0069	1	1.4	-0.4	0.0115
0	1.4	0	0.0087	-1.2	-1	0.4	0.0058	-1.2	1.4	-0.4	-0.0062
0	-1	0	0.0135	1	0	0.4	0.0165	1	0	-0.4	0.0097
1	0	0	0.0124	-1.2	0	0.4	0.0095	-1.2	0	-0.4	0.0007
-1.2	0	0	-0.0091	1	1.4	0	0.0229	1	-1	-0.4	0.0032
0	1.4	0.4	0.0050	-1.2	1.4	0	-0.0037	0	-1	-0.4	0.0167
0	-1	0.4	0.0191	1	-1	0	0.0142	-1.2	-1	-0.4	0.0047

B.0.6. Correlation factor between Photon $|\eta|$ and $\Delta\phi(\ell,\ell)$

Sample			Correlation	Sample			Correlation	Sample			Correlation
ctW	ctZ	ctG	factor	ctW	ctZ	ctG	factor	ctW	ctZ	ctG	factor
0	0	0	0.0067	1	1.4	0.4	-0.0213	-1.2	-1	0	0.0109
0	0	0.4	0.0029	1	-1	0.4	0.0065	0	1.4	-0.4	-0.0027
0	0	-0.4	0.0011	-1.2	1.4	0.4	0.0137	1	1.4	-0.4	-0.0116
0	1.4	0	-0.0080	-1.2	-1	0.4	0.0050	-1.2	1.4	-0.4	0.0208
0	-1	0	-0.0002	1	0	0.4	0.0136	1	0	-0.4	0.0023
1	0	0	0.0117	-1.2	0	0.4	-0.0047	-1.2	0	-0.4	0.0032
-1.2	0	0	0.0050	1	1.4	0	-0.0045	1	-1	-0.4	0.0007
0	1.4	0.4	-0.0140	-1.2	1.4	0	0.0185	0	-1	-0.4	-0.0049
0	-1	0.4	0.0085	1	-1	0	0.0086	-1.2	-1	-0.4	-0.0058

B.0.7. Correlation factor between $\Delta R_{min}(\gamma,\ell)$ and $\Delta\eta(\ell,\ell)$

Sample			Correlation	Sample			Correlation	Sample			Correlation
ctW	ctZ	ctG	factor	ctW	ctZ	ctG	factor	ctW	ctZ	ctG	factor
0	0	0	0.136	1	1.4	0.4	0.151	-1.2	-1	0	0.150
0	0	0.4	0.143	1	-1	0.4	0.133	0	1.4	-0.4	0.167
0	0	-0.4	0.150	-1.2	1.4	0.4	0.176	1	1.4	-0.4	0.146
0	1.4	0	0.168	-1.2	-1	0.4	0.152	-1.2	1.4	-0.4	0.176
0	-1	0	0.133	1	0	0.4	0.131	1	0	-0.4	0.133
1	0	0	0.138	-1.2	0	0.4	0.174	-1.2	0	-0.4	0.176
-1.2	0	0	0.170	1	1.4	0	0.138	1	-1	-0.4	0.143
0	1.4	0.4	0.176	-1.2	1.4	0	0.177	0	-1	-0.4	0.137
0	-1	0.4	0.125	1	-1	0	0.151	-1.2	-1	-0.4	0.146

B.0.8. Correlation factor between $\Delta R_{min}(\gamma,\ell)$ and $\Delta\phi(\ell,\ell)$

Sample			Correlation	Sample			Correlation	Sample			Correlation
ctW	ctZ	ctG	factor	ctW	ctZ	ctG	factor	ctW	ctZ	ctG	factor
0	0	0	-0.310	1	1.4	0.4	-0.313	-1.2	-1	0	-0.315
0	0	0.4	-0.313	1	-1	0.4	-0.405	0	1.4	-0.4	-0.351
0	0	-0.4	-0.314	-1.2	1.4	0.4	-0.409	1	1.4	-0.4	-0.318
0	1.4	0	-0.352	-1.2	-1	0.4	-0.306	-1.2	1.4	-0.4	-0.413
0	-1	0	-0.335	1	0	0.4	-0.343	1	0	-0.4	-0.352
1	0	0	-0.336	-1.2	0	0.4	-0.344	-1.2	0	-0.4	-0.351
-1.2	0	0	-0.347	1	1.4	0	-0.323	1	-1	-0.4	-0.402
0	1.4	0.4	-0.335	-1.2	1.4	0	-0.419	0	-1	-0.4	-0.329
0	-1	0.4	-0.334	1	-1	0	-0.400	-1.2	-1	-0.4	-0.312

B.0.9. Correlation factor between $\Delta R_{min}(\gamma,\ell)$ and $\Delta\phi(\ell,\ell)$

Sample			Correlation	Sample			Correlation	Sample			Correlation
ctW	ctZ	ctG	factor	ctW	ctZ	ctG	factor	ctW	ctZ	ctG	factor
0	0	0	-0.0318	1	1.4	0.4	-0.0328	-1.2	-1	0	-0.0281
0	0	0.4	-0.0324	1	-1	0.4	-0.0473	0	1.4	-0.4	-0.0414
0	0	-0.4	-0.0285	-1.2	1.4	0.4	-0.0478	1	1.4	-0.4	-0.0336
0	1.4	0	-0.0327	-1.2	-1	0.4	-0.0340	-1.2	1.4	-0.4	-0.0492
0	-1	0	-0.0279	1	0	0.4	-0.0312	1	0	-0.4	-0.0308
1	0	0	-0.0344	-1.2	0	0.4	-0.0361	-1.2	0	-0.4	-0.0438
-1.2	0	0	-0.0459	1	1.4	0	-0.0256	1	-1	-0.4	-0.0488
0	1.4	0.4	-0.0446	-1.2	1.4	0	-0.0541	0	-1	-0.4	-0.0317
0	-1	0.4	-0.0392	1	-1	0	-0.0484	-1.2	-1	-0.4	-0.0391

Bibliography

[1] J. J. Thomson, *Cathode rays*, The London, Edinburgh, and Dublin Philosophical Magazine and Journal of Science **44(269)**, 293 (1897)

[2] E. Rutherford, *The scattering of α and β particles by matter and the structure of the atom*, The London, Edinburgh, and Dublin Philosophical Magazine and Journal of Science **21(125)**, 669 (1911)

[3] N. Bohr, *On the Constitution of Atoms and Molecules*, Phil. Mag. Ser.6 **26**, 1 (1913)

[4] J. Chadwick, *Possible Existence of a Neutron*, Nature **129**, 312 (1932)

[5] J. C. Street, E. C. Stevenson, *New Evidence for the Existence of a Particle of Mass Intermediate Between the Proton and Electron*, Phys. Rev. **52**, 1003 (1937)

[6] S. L. Glashow, *Partial Symmetries of Weak Interactions*, Nucl. Phys. **22**, 579 (1961)

[7] S. Weinberg, *A Model of Leptons*, Phys. Rev. Lett. **19**, 1264 (1967)

[8] A. Salam, *Weak and Electromagnetic Interactions*, ed. Nobel Symposium No. 8 (Almqvist & Wiksell, Stockholm, 1968)

[9] S. L. Glashow, J. Iliopoulos, L. Maiani, *Weak Interactions with Lepton-Hadron Symmetry*, Phys. Rev. D **2**, 1285 (1970)

[10] H. Georgi, S. L. Glashow, *Unified Weak and Electromagnetic Interactions without Neutral Currents*, Phys. Rev. Lett. **28**, 1494 (1972)

[11] H. D. Politzer, *Reliable Perturbative Results for Strong Interactions*, Phys. Rev. Lett. **30**, 1346 (1973)

[12] H. D. Politzer, *Asymptotic Freedom: An Approach to Strong Interactions*, Phys. Rept. **14**, 129 (1974)

[13] D. J. Gross, F. Wilczek, *Asymptotically Free Gauge Theories*, Phys. Rev. D **8**, 3633 (1973)

[14] G. 't Hooft, *Renormalizable Lagrangians For Massive Yang-Mills Fields*, Nucl. Phys. B **35**, 167 (1971)

[15] G. 't Hooft, M. Veltmann, *Regularization And Renormalization Of Gauge Fields*, Nucl. Phys. B **44**, 189 (1972)

[16] G. 't Hooft, M. Veltmann, *Combinatorics of gauge fields*, Nucl. Phys. B **50**, 318 (1972)

[17] DØ Collaboration, *Observation of the Top Quark*, Phys. Rev. Lett. **74**, 2632 (1995)

[18] CDF Collaboration, *Evidence for top quark production in $\bar{p}p$ collisions at $\sqrt{s} = 1.8$ TeV*, Phys. Rev. Lett. **73**, 225 (1994)

[19] ATLAS Collaboration, *Observation of a new particle in the search for the Standard Model Higgs boson with the ATLAS detector at the LHC*, Phys. Lett. **B716**, 1 (2012)

[20] CMS Collaboration, *Observation of a New Boson at a Mass of 125 GeV with the CMS Experiment at the LHC*, Phys. Lett. **B716**, 30 (2012)

[21] ATLAS Collaboration, *Measurement of the Higgs boson mass in the $H \to ZZ^* \to 4\ell$ and $H \to \gamma\gamma$ channels with $\sqrt{s} = 13$ TeV pp collisions using the ATLAS detector*, Phys. Lett. **B784**, 345 (2018)

[22] ATLAS Collaboration, *Study of the spin and parity of the Higgs boson in diboson decays with the ATLAS detector*, EPJ **C75(10)**, 476 (2015)

[23] P. W. Higgs, *Broken Symmetries, Massless Particles and Gauge Fields*, Phys. Lett. **12**, 132 (1964)

[24] F. Englert, R. Brout, *Broken Symmetry and the Mass of Gauge Vector Mesons*, Phys. Rev. Lett. **13**, 321 (1964)

[25] M. Kobayashi, T. Maskawa, *CP Violation in the Renormalizable Theory of Weak Interaction*, Prog. Theor. Phys. **49**, 652 (1973)

[26] J. W. Cronin, et al., *Evidence for the 2π Decay of the K_2^0 Meson*, Phys. Rev. Lett. **13**, 138 (1964)

[27] M. L. Perl, et al., *Evidence for Anomalous Lepton Production in $e^+ - e^-$ Annihilation*, Phys. Rev. Lett. **35**, 1489 (1975)

[28] S. W. Herb, et al., *Observation of a Dimuon Resonance at* 9.5 GeV *in* 400 GeV *Proton-Nucleus Collisions*, Phys. Rev. Lett. **39**, 252 (1977)

[29] CDF Collaboration, *Observation of Top Quark Production in $p\bar{p}$ Collisions with the Collider Detector at Fermilab*, Phys. Rev. Lett. **74**, 2626 (1995)

[30] ATLAS Collaboration, *Measurement of the top quark mass in the $t\bar{t} \to$ lepton+jets channel from $\sqrt{s} = 8$ TeV ATLAS data and combination with previous results*, EPJ **C79(4)**, 290 (2019)

[31] I. I. Y. Bigi, et al., *Production and decay properties of ultraheavy quarks*, Phys. Lett. B **181**, 157 (1986)

[32] R. D. Ball, et al. (NNPDF), *Parton distributions from high-precision collider data*, EPJ C **C77(10)**, 663 (2017)

[33] J. C. Collins, D. E. Soper, *The Theorems of Perturbative QCD*, Ann. Rev. Nucl. Part. Sci. **37**, 383 (1987)

[34] Y. Fukuda, et al. (Super-Kamiokande Collaboration), *Evidence for Oscillation of Atmospheric Neutrinos*, Phys. Rev. Lett. **81**, 1562 (1998)

[35] A. D. Sakharov, *Violation of CP Invariance, C asymmetry, and baryon asymmetry of the universe*, Pisma Zh. Eksp. Teor. Fiz. **5**, 32 (1967)

[36] L. Bergstroem, *Non-baryonic dark matter: observational evidence and detection methods*, Reports on Progress in Physics **63(5)**, 793 (2000)

[37] P. F. Smith, J. D. Lewin, *Dark matter detection*, Physics Reports **187(5)**, 203 (1990)

[38] E. J. Copeland, M. Sami, S. Tsujikawa, *Dynamics of dark energy*, International Journal of Modern Physics D **15(11)**, 1753 (2006)

[39] T. G. Rizzo, *Pedagogical introduction to extra dimensions*, eConf **C040802**, L013 (2004)

[40] H. Georgi, *Effective field theory*, Annual review of nuclear and particle science **43(1)**, 209 (1993)

[41] D. J. E. Marsh, *Axion Cosmology*, Phys. Rept. **643**, 1 (2016)

[42] D. Barducci, et al., *Interpreting top-quark LHC measurements in the standard-model effective field theory* (2018), 1802.07237

[43] B. Grzadkowski, et al., *Dimension-six terms in the standard model lagrangian*, JHEP **2010(10)**, 85 (2010)

[44] O. B. Bylund, et al., *Probing top quark neutral couplings in the Standard Model Effective Field Theory at NLO in QCD*, JHEP **2016(5)**, 52 (2016)

[45] L. R. Evans, *The Large Hadron Collider (LHC)*, IEEE Trans. Appl. Supercond. **14**, 147 (2004)

[46] Airapetian, et al., *ATLAS detector and physics performance: Technical Design Report, 1*, CERN-LHCC-99-014, ATLAS-TDR-014 (1999)

[47] CMS Collaboration, *CMS physics technical design report, volume II: physics performance*, Journal of Physics G: Nuclear and Particle Physics **34(6)**, 995 (2007)

[48] K. Aamodt, et al., *The ALICE experiment at the CERN LHC*, Journal of Instrumentation **3(08)**, S08002 (2008)

[49] A. Jr, et al., *The LHCb detector at the LHC*, Journal of Instrumentation **3(08)**, S08005 (2008)

[50] ATLAS Collaboration, *The Run-2 ATLAS Trigger System*, Technical Report ATL-DAQ-PROC-2016-003, CERN, Geneva (2016)

[51] J. Alwall, others., *The automated computation of tree-level and next-to-leading order differential cross sections, and their matching to parton shower simulations*, JHEP **2014(7)**, 79 (2014)

[52] N. P. Hartland, et al., *A Monte Carlo global analysis of the Standard Model Effective Field Theory: the top quark sector*, JHEP **2019(4)**, 100 (2019)

[53] ATLAS Collaboration, *Measurements of inclusive and differential cross-sections of $t\bar{t}\gamma$ production in the $e\mu$ channel at 13 TeV with the ATLAS detector*, ATLAS-CONF-2019-042 (2019)

[54] G. Bevilacqua, others., *Hard photons in hadroproduction of top quarks with realistic final states*, JHEP **2018(10)**, 158 (2018)

[55] N. Castro, et al., *EFTfitter: a tool for interpreting measurements in the context of effective field theories*, EPJ C **76(8)**, 432 (2016)

[56] A. Caldwell, D. Kollar, K. Kroninger, *BAT: The Bayesian Analysis Toolkit*, Comput. Phys. Commun. **180**, 2197 (2009)

[57] S. BiÃmann, et al., *Constraining top-quark couplings combining top-quark and BB decay observables*, EPJ C **80(2)** (2020)